

1 Using atmospheric observations to quantify annual biogenic carbon 2 dioxide fluxes on the Alaska North Slope

3 Luke D. Schiferl^{1,2}, Jennifer D. Watts³, Erik J. L. Larson⁴, Kyle A. Arndt^{3,5,6}, Sébastien C. Biraud⁷,
4 Eugénie S. Euskirchen⁸, Jordan P. Goodrich^{5,9}, John M. Henderson¹⁰, Aram Kalhori^{5,11}, Kathryn
5 McKain^{12,13}, Marikate E. Mountain¹⁰, J. William Munger², Walter C. Oechel^{5,14}, Colm Sweeney¹²,
6 Yonghong Yi^{15,16}, Donatella Zona^{5,17}, and Róisín Commane^{1,18}

7 ¹Lamont-Doherty Earth Observatory, Columbia University, Palisades, New York, USA.

8 ²Harvard John A. Paulson School of Engineering and Applied Sciences, Cambridge, Massachusetts, USA.

9 ³Woodwell Climate Research Center, Falmouth, Massachusetts, USA.

10 ⁴Department of Organismic and Evolutionary Biology, Harvard University, Cambridge, Massachusetts, USA.

11 ⁵Department of Biology, San Diego State University, San Diego, California, USA.

12 ⁶Earth Systems Research Center, Institute for the Study of Earth, Oceans, and Space, University of New Hampshire, Durham,
13 New Hampshire, USA.

14 ⁷Lawrence Berkeley National Laboratory, Berkeley, California, USA.

15 ⁸Institute of Arctic Biology, University of Alaska Fairbanks, Fairbanks, Alaska, USA.

16 ⁹Ministry for the Environment, Wellington, New Zealand.

17 ¹⁰Atmospheric and Environmental Research, Inc., Lexington, Massachusetts, USA.

18 ¹¹GFZ German Research Centre for Geosciences, Potsdam, Germany.

19 ¹²Global Monitoring Laboratory, Earth System Research Laboratories, NOAA, Boulder, Colorado, USA.

20 ¹³Cooperative Institute for Research in Environmental Sciences, University of Colorado, Boulder, Colorado, USA.

21 ¹⁴Department of Geography, University of Exeter, Exeter, United Kingdom.

22 ¹⁵Joint Institute for Regional Earth System Science and Engineering, University of California, Los Angeles, California, USA.

23 ¹⁶College of Surveying and Geo-Informatics, Tongji University, Shanghai, China.

24 ¹⁷Department of Animal and Plant Sciences, University of Sheffield, Western Bank, Sheffield, United Kingdom.

25 ¹⁸Department of Earth and Environmental Sciences, Columbia University, New York, New York, USA.

26 *Correspondence to:* Luke D. Schiferl (schiferl@ldeo.columbia.edu)

27 **Abstract.** The continued warming of the Arctic could release vast stores of carbon into the atmosphere from high-latitude
28 ecosystems, especially from thawing permafrost. Increasing uptake of carbon dioxide (CO₂) by vegetation during longer
29 growing seasons may partially offset such release of carbon. However, evidence of significant net annual release of carbon
30 from site-level observations and model simulations across tundra ecosystems has been inconclusive. To address this knowledge
31 gap, we combined top-down observations of atmospheric CO₂ concentration enhancements from aircraft and a tall tower,
32 which integrate ecosystem exchange over large regions, with bottom-up observed CO₂ fluxes from tundra environments and
33 found that the Alaska North Slope is not a consistent net source or net sink of CO₂ to the atmosphere (ranging from -6 to +6
34 TgC yr⁻¹ for 2012–2017). Our analysis suggests that significant biogenic CO₂ fluxes from unfrozen terrestrial soils, and likely
35 inland waters, during the early cold season (September–December) are major factors in determining the net annual carbon
36 balance of the North Slope, implying strong sensitivity to the rapidly warming freeze-up period. At the regional level, we find
37 no evidence for previously reported large late cold season (January–April) CO₂ emissions to the atmosphere during the study

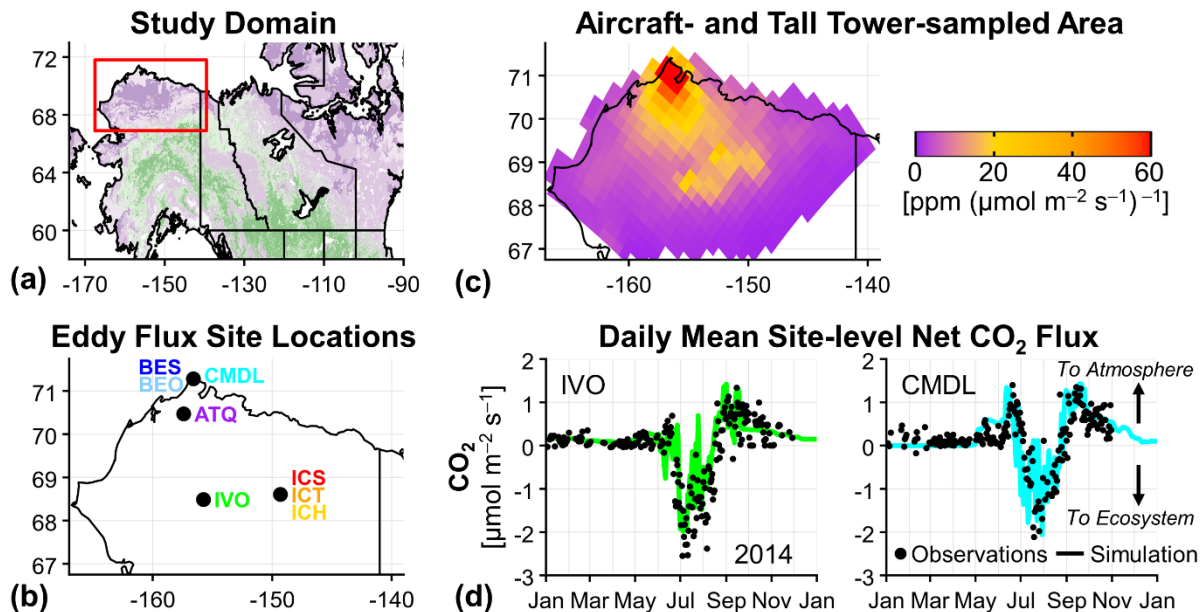
38 period. Despite the importance of the cold season CO₂ emissions to the annual total, the interannual variability of the net CO₂
39 flux is driven by the variability in growing season fluxes. During the growing season, the regional net CO₂ flux is also highly
40 sensitive to the distribution of tundra vegetation types throughout the North Slope. This study shows that quantification and
41 characterization of year-round CO₂ fluxes from the heterogeneous terrestrial and aquatic ecosystems in the Arctic using both
42 site-level and atmospheric observations is important to accurately project the earth system response to future warming.

43 **1 Introduction**

44 The Arctic surface air temperature is warming at twice the rate of the global average (Box et al., 2019; Meredith et al., 2019).
45 Continued thawing of Arctic permafrost has the potential to release vast stores of carbon into the atmosphere, thereby further
46 accelerating warming (Schuur et al., 2015; Hugelius et al., 2014). In the biosphere, the net CO₂ flux is the balance between
47 uptake of CO₂ by vegetation through photosynthesis (negative net CO₂ flux indicates removal from the atmosphere) and release
48 of CO₂ into the atmosphere by plant and microbial respiration (positive net CO₂ flux indicates a source to the atmosphere).
49 Arctic growing seasons are short (~3 months), and the long, cold season dominates the seasonal cycle. The transition between
50 the growing and cold seasons is marked by the soil zero-curtain period, when belowground temperatures of the active layer
51 above frozen permafrost remain near freezing; the active layer is insulated by snow and ice at the surface and warmed by the
52 latent heat release of freezing water (Outcalt et al., 1990). During the zero-curtain period, soil respiration can remain active in
53 deeper soils for weeks to months after the end of the growing season (Zona et al., 2016; Romanovsky and Osterkamp, 2000).
54 As the climate warms, the active layer above permafrost deepens, thawed soils become wetter, a larger volume of soil remains
55 unfrozen for a longer period of time, and the duration of the zero-curtain period plays an increasingly important role in
56 determining the net carbon exchange in Arctic ecosystems (Kim et al., 2012; Arndt et al., 2019). Recent work has shown a
57 significant cold season source of CO₂ from Arctic ecosystems, including more than 70% increase in October–December CO₂
58 concentration enhancements in the past 40 years, consistent with an increase in cold season respiration, which is not well
59 represented in earth system models (Commane et al., 2017; Natali and Watts et al., 2019). Neglecting these processes could
60 lead to large underestimation of CO₂ emissions, biasing current and future climate projections.

61 Tundra ecosystems, characterized by frozen soils covered in low shrubs, sedges, grasses, and mosses, make up
62 approximately 50% of the Arctic landscape (Raynolds et al., 2019). Lacking trees, the magnitude of net CO₂ uptake in tundra
63 during the growing season is relatively small and may be offset by emissions from respiration that can continue well into the
64 cold season (Watts et al., 2021). In the past, year-round CO₂ flux measurements from tundra ecosystems were rare due to
65 difficulties in maintaining instrumentation under remote and extreme cold conditions (Euskirchen et al., 2017; Kittler et al.,
66 2017; Goodrich et al., 2016). Long-term year-round CO₂ concentration measurements have been made in the Arctic at a small
67 number of tall towers, which have been situated to sample clean marine air off the ocean (Jeong et al., 2018; Worthy et al.,
68 2009). While aircraft provide greater spatial coverage over land than these towers, they tend to operate for short durations, and
69 their temporal coverage is limited by weather and visibility during the cold season (Chang et al., 2014; Commane et al., 2017;

70 Miller et al., 2016). However, the recent increase in availability of observations of gas fluxes and concentrations within a
 71 particular tundra region, the Alaska North Slope (Fig. 1a), is making it possible to better conduct year-round multi-scale
 72 assessments of tundra ecosystems, with the aim of improving our understanding of CO₂ sink/source activity and carbon budgets
 73 in these environments.



74

75 **Figure 1.** Alaska North Slope study region, eddy flux site locations, area sampled by aircraft and tower, and example results from the eddy
 76 flux site measurement-model comparison. (a) North Slope region (red box) within Alaska and northwestern Canada. Tundra areas shown in
 77 purple and boreal forest areas shown in green (Luus et al., 2017). (b) Location of eddy flux measurement sites on the Alaska North Slope
 78 used in this analysis. (c) Ten-day WRF-STILT footprints used to sample CO₂ flux models, summed for all aircraft and tall tower CO₂
 79 observations used in this analysis. Colors represent values greater than 0 and are saturated at 60 ppm (μmol m⁻² s⁻¹)⁻¹. Maximum value near
 80 Utqiagvik, Alaska is 324 ppm (μmol m⁻² s⁻¹)⁻¹. (d) Timeseries of observed (black dots) and simulated (colored lines) site-level daily mean
 81 net CO₂ flux for 2014 at IVO (left) and CMDL (right) eddy flux measurement sites, where site-level TVPRM net CO₂ flux simulations are
 82 driven by NARR meteorology and the CSIF SIF product. Positive net CO₂ flux values indicate CO₂ fluxes into the atmosphere throughout
 83 this study. A comparison for all eight eddy flux sites is provided in Fig. S1 in Supplement.

84 Currently, observations and models do not agree on the sign of the annual net CO₂ flux across the Alaska North Slope
 85 region. Site-level measurements and atmospheric observations suggest this region is a net CO₂ source (Commane et al., 2017;
 86 Oechel et al., 2014; Euskirchen et al., 2017). However, a comparison of process-based models of the North Slope found large
 87 variability in the sign and magnitude of the net CO₂ flux with an approximately neutral regional annual net CO₂ flux multi-
 88 model mean of -3.5 ± 67 TgC yr⁻¹ (Fisher et al., 2014). In a more recent study, Tao et al. (2021) found an annual net CO₂ flux
 89 range of -9 to 12 TgC yr⁻¹ for the years 2010–2016, with only 2014 being an annual net CO₂ source. Extrapolating from site-
 90 level CO₂ flux measurements to regional budgets is difficult due to the extreme heterogeneity of tundra ecosystems in the
 91 North Slope and a lack of spatial and seasonal representativeness by existing flux monitoring sites (Pallandt et al., 2022).

92 In this study, we compare *bottom-up* flux estimates with *top-down* atmospheric observations from aircraft and a tall
 93 tower using an integrated modeling approach to quantify the CO₂ budget sign and magnitude of the Alaska North Slope. Our

94 framework first applies a bottom-up approach to understand Arctic tundra ecosystem CO₂ fluxes, constrained by site-level
95 observations, using an empirical model ensemble of CO₂ fluxes derived from eddy flux measurements representing varied
96 tundra ecosystems within the region. We then apply top-down information gained from regional CO₂ concentration
97 enhancement observations measured by a tall tower and aircraft, which sample the atmosphere-biosphere exchange throughout
98 the Alaska North Slope, to evaluate the range of potential CO₂ fluxes identified by the bottom-up model ensemble for 2012–
99 2017. This evaluation also identifies the ecosystem parameterizations, vegetation distributions, and environmental drivers that
100 best characterize the observed spatial and temporal distribution of biogenic CO₂ in the atmosphere across the region. By
101 developing regional CO₂ budgets constrained by both atmospheric observations and ecosystem environmental responses, we
102 can better project how Arctic tundra ecosystems will respond to climate change on annual and decadal timescales.

103 **2 Materials and methods**

104 **2.1 Observed CO₂ concentrations and fluxes on the Alaska North Slope**

105 **2.1.1 Atmospheric CO₂ concentration observations**

106 We use a suite of CO₂ concentration observations from various sources on the North Slope for our analysis. The United States
107 (US) National Oceanic and Atmospheric Administration (NOAA) Barrow Atmospheric Baseline Observatory (BRW) tall
108 tower near Utqiagvik, Alaska has made continuous in situ CO₂ concentration measurements since 1973 (Sweeney et al., 2016).
109 The US Department of Energy (DOE) Atmospheric Radiation Measurement Climate Research Facility Airborne Carbon
110 Measurements V (ARM-ACME V) airborne campaign measured CO₂ concentrations sub-weekly from June to September
111 2015 over the North Slope (Biraud et al., 2016; Tadić et al., 2021). The US National Aeronautics and Space Administration
112 (NASA) Arctic-Boreal Vulnerability Experiment (ABoVE) Arctic Carbon Atmospheric Profiles (Arctic-CAP) airborne
113 campaign flew throughout Alaska and northwestern Canada approximately every month from May to November 2017
114 (Sweeney and McKain, 2019; Sweeney et al., 2022). CO₂ concentration observations from the NASA Carbon in Arctic
115 Reservoirs Vulnerability Experiment (CARVE) flights for 2012–2014 are incorporated into the Commane et al. (2017)
116 optimized CO₂ fluxes used in our analysis below. The NOAA/US Coast Guard collaborative Alaska Coast Guard (ACG)
117 flights have also made aircraft CO₂ concentration measurements in the region, but these coastal flights observe only limited
118 spatial coverage of the North Slope, and we do not use them here.

119 For the NOAA BRW tower, we use hourly CO₂ concentration observations with wind direction from the land (135°–
120 202.5° clockwise w.r.t. north) and ocean sectors (0°–45°), avoiding Utqiagvik anthropogenic activity, with wind speed > 2.5
121 m s⁻¹ (Fig. S2) (Commane et al., 2017; Sweeney et al., 2016). We only use land sector observations from the cold season
122 (defined here as September–April) since seasonal wind patterns do not favor transport from those directions during the growing
123 season (defined here as May–August). For the ARM-ACME V and ABoVE Arctic-CAP aircraft campaign observations, we
124 group averaged sampling points into 50 m vertical bins after removing data influenced by combustion sources such as

125 anthropogenic activity and biomass burning events. These combustion sources of CO₂ are expected to be small (<1 TgC yr⁻¹
126 on the North Slope, see Table S1) during our study period. They are not accounted for in biogenic CO₂ flux models, however,
127 and must be removed from our analysis when observed. We remove time periods with elevated carbon monoxide (CO)
128 concentration above 150 ppb, as in Chang et al. (2014) and Commane et al. (2017), which indicates local combustion sources.
129 Time periods with highly variable CO concentrations ($\Delta\text{CO} > 40$ ppb) indicate complex mixing of more remote combustion
130 sources and are also removed (Chang et al., 2014). The remaining grouped sampling points correspond to the available
131 Lagrangian atmospheric transport modeling system simulations (WRF-STILT (Henderson et al., 2015), see below): ARM-
132 ACME V points are calculated every 50 m vertically below 1 km, every 100 m vertically above 1 km, and every 10 km
133 horizontally from 1 s observations, and ABoVE Arctic-CAP points are matched every 20 s from averaged 10 s observations.
134 To ensure these points observe the Alaska North Slope, we only use points with at least 70% of the total 10-day WRF-STILT
135 simulated surface influence occurring in our regional domain.

136 **2.1.2 Eddy covariance CO₂ flux tower observations**

137 We also use up to five years (2013–2017) of year-round observations of net CO₂ flux from eight eddy covariance tower sites
138 (for 32 total site-years) representing an array of tundra ecosystems throughout the Alaska North Slope (Figs. 1b, S1, Table S2
139 in Supplement). These half-hourly eddy flux measurements of net CO₂ flux are not gap-filled to avoid introducing additional
140 uncertainties. Three of the sites are located near Imnavait Creek along a wetness gradient from valley to hilltop: wet sedge
141 tundra (ICS), moist acidic tussock tundra (ICT) and dry heath tundra (ICH) (Euskirchen et al., 2017, 2012). The other sites
142 include tussock tundra at Ivotuk (IVO), wet polygonised tundra at Atqasuk (ATQ), and three sites near Utqiagvik: wetland
143 tundra (BES), wet polygonised tundra (BEO), and moist tundra (CMDL) (Zona et al., 2016; Arndt et al., 2020).

144 **2.2 Observed atmospheric CO₂ concentration enhancement calculation**

145 We calculate the observed *top-down* atmospheric CO₂ concentration enhancement (ΔCO_2) for the North Slope region for every
146 land-sector hour at the NOAA BRW tower and for every 50 m of vertical distance transited during the airborne campaigns
147 (ARM-ACME V, ABoVE Arctic-CAP). The observed ΔCO_2 [units: ppm] generated by the North Slope ecosystem is
148 calculated relative to the background concentration without influence from this region such that:

$$149 \quad \text{observed } \Delta\text{CO}_2 = \text{observed } [\text{CO}_2] - \text{background } [\text{CO}_2] \quad (1)$$

150 following previous work (Sweeney et al., 2016; Commane et al., 2017; Jeong et al., 2018).

151 The background CO₂ concentrations at the NOAA BRW tower are determined by smoothing the 10-day mean of the
152 observed ocean sector concentrations using spline fitting to produce a daily CO₂ background concentration. We calculate the
153 uncertainty of these background concentrations by both 1) varying the starting hour of the 10-day mean calculation prior to
154 spline fitting and 2) randomly sub-selecting 50% the ocean sector concentrations 1000 times. The interval that contains 95%
155 of these 240,000 fits represents our daily background uncertainty. Figure S2 shows the ocean sector concentrations, resulting
156 background concentration, and uncertainty described here.

157 To determine the background CO₂ concentrations for the ARM-ACME V and ABoVE Arctic-CAP aircraft
158 campaigns, we isolate aircraft observations without surface influence from the North Slope using the WRF-STILT footprints
159 as done for larger regions in Chang et al. (2014) and Commane et al. (2017). These observed CO₂ concentrations represent the
160 state of the air before it interacts with the surface in the study region. The regional backgrounds vary by the direction from
161 which the air enters the domain. For example, the backgrounds from the south and from over land generally experience CO₂
162 drawdown prior to those from over the Arctic Ocean. The time- and directional-dependent backgrounds we use are shown in
163 Fig. S3. We apply the uncertainty from the NOAA BRW tower background to the aircraft backgrounds as a reasonable
164 representation of the variability associated with available background CO₂ concentration data.

165 **2.3 Simulated atmospheric CO₂ concentration enhancement calculation**

166 To understand how landscape interactions with the atmosphere (through CO₂ flux) influenced the observed CO₂ concentrations
167 across space and time, we calculate the corresponding simulated ΔCO₂ [units: ppm] by transporting *bottom-up* biogenic CO₂
168 fluxes to each observation site such that:

$$169 \quad \text{simulated } \Delta\text{CO}_2 = \text{simulated CO}_2 \text{ flux} \times \text{simulated footprint} \quad (2)$$

170 In this calculation, we multiply the hourly simulated CO₂ flux [$\mu\text{mol CO}_2 \text{ m}^{-2} \text{ s}^{-1}$] by the footprint [ppm ($\mu\text{mol CO}_2 \text{ m}^{-2} \text{ s}^{-1}$)⁻¹]
171 ¹] for that hour starting at the observation point, backward in time for each hour up to ten days, where the footprint quantifies
172 the influence of the land surface on the concentration observed at a measurement point. The simulated ΔCO₂ is then the sum
173 of these hours.

174 We use expected CO₂ fluxes based on a variety of bottom-up model approaches which represent North Slope
175 ecosystems. Year-round bottom-up estimates of net CO₂ fluxes (defined by the models as net ecosystem exchange, NEE) are
176 obtained from the Tundra Vegetation Photosynthesis and Respiration Model (TVPRM) ensemble, and from existing model
177 output from Luus et al. (2017) and Commane et al. (2017). Independent bottom-up estimates of belowground CO₂ emissions
178 (= NEE) for the cold season (net CO₂ uptake = 0) were obtained from Natali and Watts et al. (2019) and Watts et al. (2021).
179 The TVPRM model ensemble development process is described in Sect. 2.4, and the other CO₂ flux models, including their
180 native spatial and temporal resolutions, are listed in Table S3.

181 The footprints are generated by the Lagrangian atmospheric transport modeling system, WRF-STILT (Stochastic
182 Time-Inverted Lagrangian Transport model driven by Weather Research and Forecasting model meteorology (Henderson et
183 al., 2015)). In this system, WRF meteorological fields are first generated for the study region and time period (v3.5.1 for ARM-
184 ACME V and NOAA BRW tower footprints used here, v3.9.1 for ABoVE Arctic-CAP footprints). STILT then uses the WRF
185 meteorology to estimate the contribution of surface fluxes to the atmospheric concentration at a specified time and place, called
186 a receptor, by calculating the amount of time air (represented by a distribution of particles) spends in the lower half of the
187 boundary layer at a given location. The WRF-STILT model configurations from Henderson et al. (2015) have been used
188 extensively in numerous previous papers to study greenhouse gas fluxes using observations from aircraft and towers in Alaska,
189 including on the North Slope (e.g., Chang et al., 2014; Miller et al., 2016; Zona et al., 2016; Commane et al., 2017; Karion et

190 al., 2015; Hartery et al., 2018). An evaluation by Henderson et al. (2015) for WRF v.3.4.1 and v3.5.1 showed that their polar
 191 WRF configuration performs well against surface observations of air temperature and wind speed in Alaska and that WRF-
 192 STILT can capture the shape and approximate depth of greenhouse gases in the column. Zona et al. (2016) note that WRF
 193 planetary boundary layer ventilation rates may be biased in the fall (and winter) when heat fluxes are low, but this error is
 194 difficult to assess quantitatively. For this study, we use receptors set to correspond with the tower and aircraft CO₂
 195 concentration observations. The footprints (and their corresponding measurements) for these receptors sample air from
 196 throughout the North Slope but are concentrated more heavily toward the area around the NOAA BRW tower (Fig. 1c).

197 For calculating simulated ΔCO₂ from the TVPRM ensemble, we grid the distribution of WRF-STILT particles and
 198 their corresponding surface influence to the spatial resolution of the meteorological reanalysis products driving the model. The
 199 CO₂ flux models used for comparison to the TVPRM ensemble are similarly treated using 0.5°-gridded 10-day WRF-STILT
 200 footprints, which are available on a circumpolar grid poleward of 30°N. The simulated CO₂ fluxes from Luus et al. (2017),
 201 Natali and Watts et al. (2019), and Watts et al. (2021) are regridded to 0.5° spatial resolution. For the models by Natali and
 202 Watts et al. (2019) and Watts et al. (2021), which only estimate monthly CO₂ fluxes, we apply a constant flux for that month.
 203 Since the ends of our defined cold season (September–April) include transitional periods when some biogenic plant activity
 204 does occur (hence belowground CO₂ emissions ≠ NEE), for the Natali and Watts et al. (2019) and Watts et al. (2021) bottom-
 205 up scenarios, we add in estimates of photosynthesis and plant respiration fluxes from the TVPRM ensemble for April and
 206 September.

207 **2.4 Empirically simulated biogenic CO₂ fluxes from tundra ecosystems**

208 We develop the TVPRM as an ensemble of ecosystem-resolved models that represent a more extensive range of potential
 209 tundra ecosystem functional relationships, environmental drivers, and scaling assumptions than available from other CO₂ flux
 210 models. For this study, TVPRM generates a set of spatially and temporally varying CO₂ flux maps for a six-year period (2012–
 211 2017) at 30 × 30 km spatial and 1 hr temporal resolution for the Alaska North Slope.

212 TVPRM is driven by parameterized functional relationships for soil respiration (R_{soil}), plant respiration (R_{plant}), and
 213 photosynthesis (gross primary productivity (GPP)), which are described by:

$$214 \quad R_{\text{soil}} = \alpha_s \times T_s + \beta_s \quad (3)$$

$$215 \quad R_{\text{plant}} = \alpha_a \times T_a + \beta_a \quad (4)$$

$$216 \quad \text{GPP} = \lambda \times T_{\text{scale}} \times \text{SIF} \times \text{PAR} \times \frac{1}{1 + \frac{\text{PAR}}{\text{PAR}_0}} \quad (5)$$

$$217 \quad T_{\text{scale}} = \frac{(T_a - T_{\text{min}})(T_a - T_{\text{max}})}{(T_a - T_{\text{min}})(T_a - T_{\text{max}}) - (T_a - T_{\text{opt}})^2} \quad (6)$$

218 The simulated hourly CO₂ fluxes [units: μmol CO₂ m⁻² s⁻¹] are determined as responses to light and heat: R_{soil} is a function of
 219 near-surface soil temperature (T_s) [°C]; R_{plant} is a function of air temperature (T_a) [°C]; and GPP is a function of a temperature
 220 scalar (T_{scale}) and photosynthetically active radiation (PAR) [μmol photon m⁻² s⁻¹], with solar-induced chlorophyll fluorescence

221 (SIF) [$\text{mW m}^{-2} \text{nm}^{-1} \text{sr}^{-1}$] used to define the seasonal cycle of photosynthetic capacity. T_s depths are determined by reanalysis
222 product and listed in Table S4. T_{scale} ranges from 0 to 1 based on the position of T_a on the continuum between minimum
223 temperature ($T_{\text{min}} = 0^\circ\text{C}$), maximum temperature ($T_{\text{max}} = 40^\circ\text{C}$), and optimal temperature ($T_{\text{opt}} = 15^\circ\text{C}$). NEE is then calculated
224 as:

$$225 \quad \text{NEE} = R_{\text{soil}} + R_{\text{plant}} - \text{GPP} \quad (7)$$

226 with positive NEE values indicating a net source of CO_2 into the atmosphere and negative NEE values meaning net movement
227 of CO_2 into the biosphere. We use NEE to be synonymous with net CO_2 flux. Using SIF, which correlates to photosynthetic
228 activity (Porcar-Castell et al., 2014; Yang et al., 2015), in the modeling framework provides an advantage over indices such
229 as enhanced vegetation index (EVI) due to the limited canopy and evergreen nature of tundra ecosystems (Luus et al., 2017).

230 The parameter values (α_s , β_s , α_a , β_a , λ , PAR_0) for the site-level relationships used by TVPRM are determined first
231 using the observed net CO_2 fluxes from the eddy flux sites (see Sect. S1 in Supplement). We determine the site-level parameters
232 separately for each combination of reanalysis product (NARR (Mesinger et al., 2006) and ERA5 (Hersbach et al., 2020)),
233 which provide T_a , T_s , and PAR, and SIF product (GOME-2 (Joiner et al., 2016), GOSIF (Li and Xiao, 2019), and CSIF (Zhang
234 et al., 2018)) that will later be used to generate the regional TPVRM ensemble (Tables S4–S5, see Sects. S2–S3). Additional
235 α_s and β_s parameters are determined using T_s from the Remote Sensing driven Permafrost Model (RS-PM (Yi et al., 2019,
236 2018)) to test its implementation in TPVRM. RS-PM uses tailored input for Alaska permafrost zones, such as downscaled
237 snow depth and aircraft-observed soil dielectric constants and was developed and tested using T_s and active layer thickness
238 measurements from the North Slope. RS-PM also produces T_s at higher vertical resolution in the near-surface than the
239 reanalysis products to capture subsurface heterogeneity in unfrozen soil, which is important to represent the zero-curtain
240 throughout the freezing and thawing periods in Alaska.

241 Using the median parameter value sets for each site, we simulate the TVPRM net CO_2 flux for our study period at
242 every site location to perform a cross-site evaluation (Fig. S1). These simulated net CO_2 fluxes perform well against the net
243 CO_2 flux observations at their corresponding sites (Figs. 1d, S4, see Sect. S4). This process also identifies two distinct
244 ecosystem groups: “inland”, predominately graminoid and shrub tundra (ICS, ICT, ICH, IVO), and “coastal”, predominately
245 wetland tundra (ATQ, BES, BEO, CMDL), based on the similar simulated CO_2 flux responses to the meteorology- and SIF-
246 determined functional relationships within each group demonstrated by the cross-site evaluation (Fig. S1).

247 The net CO_2 flux for each meteorological grid box in our study domain is then calculated using the site-level
248 functional relationships for both tundra groups. These fluxes are weighted by the spatial distribution of inland and coastal
249 tundra from three different vegetation maps (CAVM (Walker et al., 2005), RasterCAVM (Raynolds et al., 2019), and ABoVE
250 LC (Wang et al., 2020), Fig. S5, Table S6, see Sect. S5) to produce the regionally scaled TVPRM net CO_2 flux. By varying
251 the choice of representative inland and coastal tundra sites, meteorological reanalysis product, vegetation map, and SIF
252 product, we generate 288 different simulations (members) of net CO_2 flux (referred to here as the unconstrained TVPRM
253 ensemble) for each grid box across the region for each of the six study years. Monthly and annual regional net CO_2 flux values
254 are calculated as the area-weighted sum of all grid boxes simulated in our domain. Notable changes since the previous iteration

255 of this empirical CO₂ flux model (Commane et al., 2017; Luus et al., 2017) include the expansion of the model to include
256 multiple ensemble members to account for variability and uncertainty in model formulation, the use of additional site-years of
257 CO₂ flux observations (with increased data coverage over the cold season), more inclusive data filtering methods, and much
258 higher temporal (1-, 4-, and 8-day rather than monthly) and spatial (0.01° and 0.05° rather than 0.5°) resolution SIF datasets.
259 We compare TVPRM to the previous model version by Luus et al. (2017) and its CARVE-informed optimization by Commane
260 et al. (2017) in Sect. 3.3.

261 **2.5 Evaluation Framework**

262 We use the atmospheric CO₂ concentration observations to evaluate the many tundra ecosystem parameterizations, vegetation
263 distributions, and environmental drivers that represent the net CO₂ flux on the North Slope over various spatial and temporal
264 scales. For this assessment, we compare the observed ΔCO₂, which are the observed CO₂ concentration changes driven by
265 regional CO₂ fluxes, with the simulated ΔCO₂ determined by combining the regional biogenic CO₂ flux models with the
266 atmospheric transport model.

267 To compare the regional observed ΔCO₂ and simulated ΔCO₂, we calculated the coefficient of determination (R²) as
268 the square of the Pearson correlation coefficient for all points. The slope (m) is determined by ordinary least squares using the
269 median of each 10% bin of ordered observed and corresponding simulated net CO₂ flux. The normalized mean bias (NMB) of
270 all points is defined as $\frac{\sum(\text{simulated} - \text{observed})}{\sum \text{observed}}$. The root-mean-square error (RMSE) of all points is defined as

$$271 \sqrt{\frac{\sum(\text{simulated} - \text{observed})^2}{n}}$$

272 These comparisons enable us to constrain the regional net CO₂ flux on the Alaska North Slope. First, we identify the
273 year-round empirically driven net CO₂ fluxes from the TVPRM ensemble (TVPRM Unconstrained) which are most consistent
274 with the CO₂ concentration observations from the two aircraft campaigns and at the tower (TVPRM Constrained) (Sects. 3.1–
275 3.2). Then, noting the large range in potential cold season CO₂ fluxes, we compare our constrained TVPRM member with CO₂
276 fluxes from previous studies (Sect. 3.3). Finally, we suggest and quantify sources of the missing CO₂ flux observed during the
277 early cold season (defined here as September–December) and incorporate those fluxes into our net CO₂ budget (TVPRM
278 Constrained + Additional Zero Curtain Emissions (ZC) and Inland Water Fluxes (IW)) (Sect. 3.4). This analysis provides a
279 unique regional net CO₂ flux quantification for the North Slope that is verified using atmospheric observations and can also
280 be explained from an ecological and physical perspective.

281 3. Results

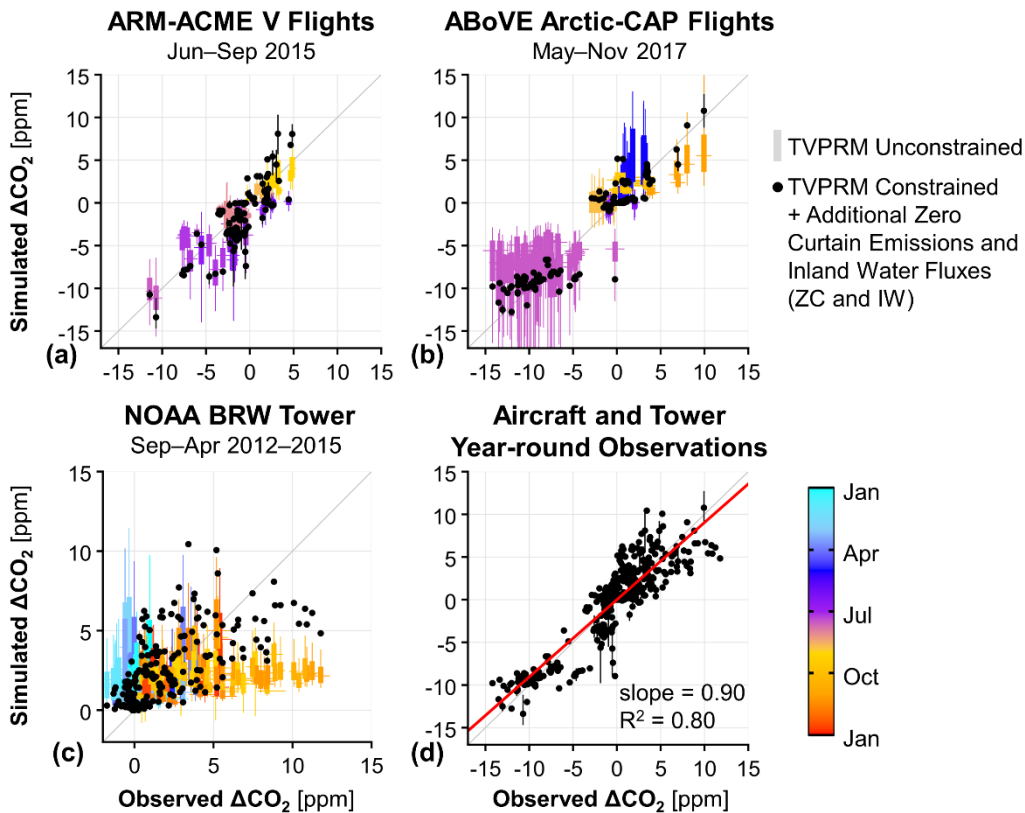
282 3.1 Evaluation of unconstrained empirical net CO₂ flux model ensemble

283 3.1.1 Using aircraft-observed CO₂ enhancements

284 The observed ΔCO_2 during the ARM-ACME V (June–September 2015) and ABoVE Arctic-CAP (May–November 2017)
285 airborne campaigns show a strong seasonal uptake pattern throughout the growing season (Figs. 2a–2b). The frequent flights
286 during ARM-ACME V (multiple flights per week) observe the transition from early to peak growing season uptake (observed
287 $\Delta\text{CO}_2 = -11$ ppm) and on into cold season respiration, which results in net CO₂ source conditions in September (+5 ppm).
288 While less frequent, the ABoVE Arctic-CAP flights begin at the end of the cold season, extend later into following cold season,
289 and cover a larger area of the North Slope. Peak growing season uptake observed by the ABoVE Arctic-CAP flights (–14 ppm)
290 is slightly stronger than for during ARM-ACME V, and by November, the ABoVE Arctic-CAP flights observe a strong CO₂
291 source throughout the North Slope (+10 ppm). The difference in observed ΔCO_2 during peak growing season uptake between
292 2015 and 2017 is likely similar to the uncertainty in the respective values and could be due to differences in areas of the North
293 Slope sampled between years.

294 The magnitude and timing of the observed net CO₂ uptake throughout the growing season is generally well
295 represented by the empirical net CO₂ flux model ensemble (TVPRM Unconstrained, Figs. 2a–2b, S6). The median coefficients
296 of determination (R^2) and ordinary least squares slopes between the observed and simulated ΔCO_2 for this time are 0.54 and
297 0.41 for ARM-ACME V and 0.82 and 0.72 for ABoVE Arctic-CAP, respectively. Only for the July observations during the
298 ABoVE Arctic-CAP campaign do many members of the CO₂ flux trend toward an underestimate of net CO₂ uptake, with all
299 points showing a much larger range in simulated values compared to ARM-ACME V. The net CO₂ release tends to be
300 overestimated by the TVPRM ensemble during the ABoVE Arctic-CAP seasonal transitions in May and September, but during
301 November the observed R_{soil} is consistently underestimated.

302 Given the large range of unconstrained representations of the regional CO₂ flux, the accuracy in simulating the aircraft
303 observed ΔCO_2 varies between TVPRM ensemble members. For example, members using the RasterCAVM vegetation map,
304 which places less coastal tundra area cover in the south (Fig. S5), produce a smaller mean July net CO₂ uptake flux (by ~1
305 $\mu\text{mol m}^{-2} \text{s}^{-1}$, Fig. S7a) throughout the southern North Slope than members using other vegetation maps (CAVM and ABoVE
306 LC), and this placement consistently underestimates the net ΔCO_2 uptake during the growing season compared to the aircraft
307 observations by 5–10 ppm (Fig. S8). Also, members driven by SIF products that integrate additional remote sensing and/or
308 meteorological data (GOSIF and CSIF) better reflect the timing and magnitude of the peak season carbon uptake in tundra
309 ecosystems than members produced by interpolated SIF retrievals (GOME-2 SIF product), which underestimate the observed
310 CO₂ uptake during July (Fig. S8).



311

312 **Figure 2.** Aircraft and tower CO₂ concentration measurements constrain year-round simulated CO₂ fluxes on the Alaska North Slope. (a)–
 313 (c) Comparison of observed and simulated ΔCO₂ during the ARM-ACME V flight campaign (a), during the ABoVE Arctic-CAP flight
 314 campaign (b), and at the NOAA BRW tower (c) for air over the Alaska North Slope. Horizontal lines indicate range of uncertainty in the
 315 NOAA BRW tower ocean sector background calculation. Vertical boxes colored by month of the year represent 50% and whiskers represent
 316 95% of ΔCO₂ values from all members of unconstrained TVPRM ensemble (see Sect. 2.4) from all binned points. Black points show values
 317 from the constrained TVPRM member with additional zero-curtain emissions (ZC) and inland water fluxes (IW) (see Sect. 3.4). For (a)–(b),
 318 observed values are vertically binned medians, and for constrained TVPRM member + ZC and IW, vertical lines contain middle 95% of
 319 ΔCO₂ values from all binned points. (d) Combined comparison of observed and simulated ΔCO₂ for all aircraft and tower points using
 320 constrained TVPRM member + ZC and IW. Shown with linear best fit (red line), slope determined by ordinary least squares, and coefficient
 321 of determination (R²) of all points (n = 455). 1:1 line shown in dark gray.

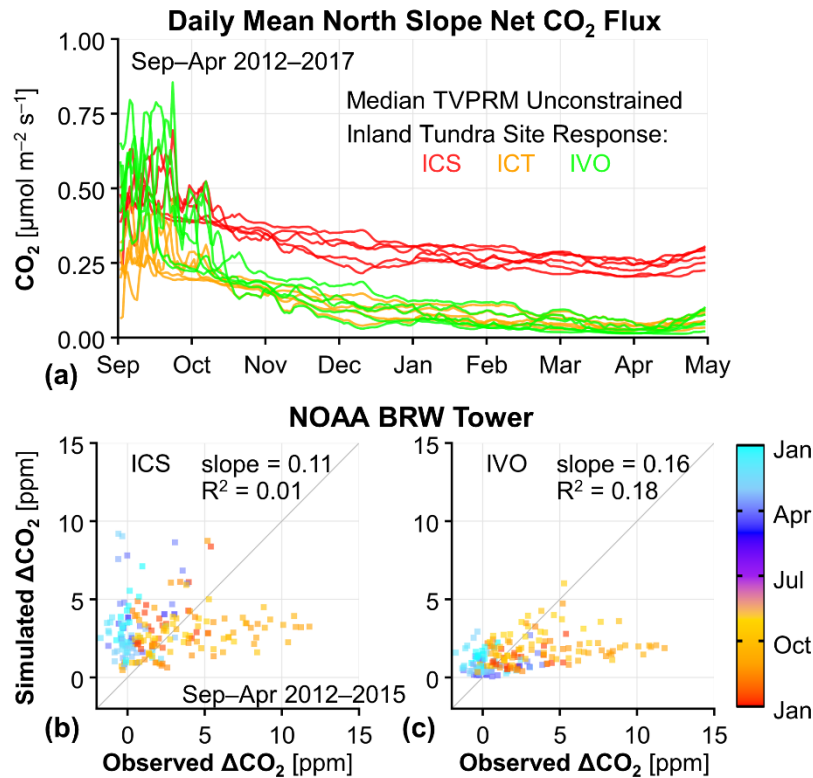
322

Using these comparisons, we identify less-representative ensemble members that generally underestimate the
 323 observed ΔCO₂ uptake during the growing season (RasterCAVM vegetation map and GOME-2 SIF product members).
 324 Removing these members from the TVPRM ensemble improves the collective performance of the remaining members during
 325 the growing season (Fig. S6), brings the median slope of agreement closer to 1 for both campaigns (improves from 0.53 to
 326 0.64 and from 0.71 to 0.94 for ARM-ACME V and ABoVE Arctic-CAP, respectively), and reduces median NMB (−0.34 to −
 327 0.03) and median RMSE (3.12 to 2.73) for ABoVE Arctic-CAP.

328 **3.1.2 Using tower-observed CO₂ enhancements**

329 As seen with the September–November aircraft data, the observed ΔCO_2 at the NOAA BRW tower (Fig. 2c) indicate that the
 330 CO₂ source to the atmosphere increases substantially from September to peak in October and November (+12 ppm) before
 331 decreasing to near zero throughout the late cold season (January–April).

332 Most of the TVPRM ensemble members substantially underestimate the observed ΔCO_2 in the early cold season
 333 (September–December) as the soils freeze, and some simulations produce too much CO₂ in the late cold season when the soils
 334 are frozen (Fig. 2c). The cold season CO₂ flux differs greatest in magnitude and spatial extent between the ensemble members
 335 parameterized for the ICS and ICT inland tundra sites (Figs. 3a, S9–S10), with a net CO₂ flux difference of $\sim 0.2 \mu\text{mol m}^{-2} \text{s}^{-1}$
 336 throughout the region (Fig. S7b).



337
 338 **Figure 3.** Cold season CO₂ emissions for inland tundra site parameterizations and comparison to tower observations. (a) Timeseries of
 339 simulated daily mean Alaska North Slope net CO₂ flux for the median of all unconstrained TVPRM ensemble members using each of three
 340 inland tundra site parameterizations: ICS (red), ICT (orange), and IVO (green). Yearly colored lines shown for Sep–Apr beginning in Sep
 341 2012 and ending in Apr 2017. Same for all eight eddy flux sites shown in Fig. S9. (b)–(c) Comparison of observed and simulated ΔCO_2 at
 342 the NOAA BRW tower for air over the North Slope using the median of all unconstrained TVPRM ensemble members for the inland tundra
 343 site parameterizations at ICS (b) and IVO (c). All points colored by day of year. Shown with slope determined by ordinary least squares and
 344 coefficient of determination (R^2) of all points ($n = 191$). 1:1 line shown in dark gray.

345 While the magnitude of CO₂ flux from ICS members better matches the observed ΔCO_2 in the early cold season than
 346 from other sites (Figs. 3b–3c, S11), the response to T_s at ICS shows only a modest decrease in CO₂ flux between the early and

347 late cold season (Fig. 3a, 32% decrease between October and March), resulting in an overestimate of the regional ΔCO_2 in the
348 late cold season. The CO_2 flux response to T_s for ICT members is similar to that for ICS but lower in magnitude, and the
349 simulated ΔCO_2 from members of neither site performs well against the observations in both the early and late cold season.
350 Therefore, ICS and ICT inland tundra responses to T_s are not representative of the regional ΔCO_2 observed at the NOAA BRW
351 tower throughout the entire cold season, and we remove those members from our TPVRM ensemble.

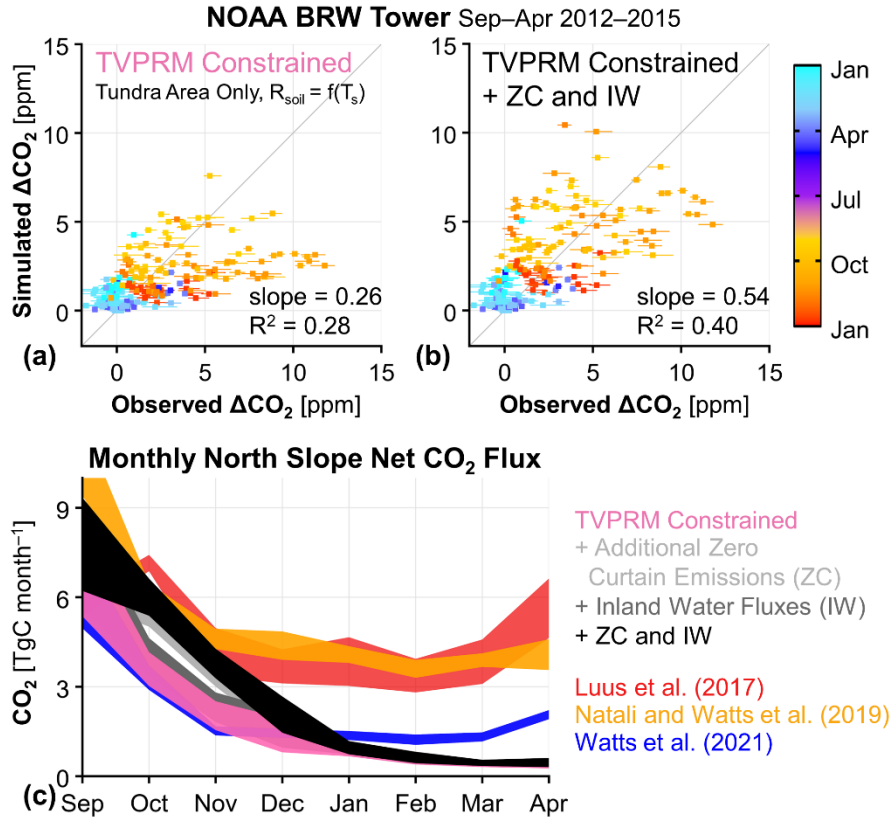
352 The observed net CO_2 fluxes at the IVO inland tundra and CMDL coastal tundra sites both show prolonged zero-
353 curtain emissions (Fig. S1) and respond strongly to T_s in the early cold season (Fig. S9). The stronger response of CO_2 fluxes
354 to T_s from the early to late cold season at IVO (Fig. 3a, 70% decrease by January) compared to at the Imnavait Creek sites
355 produces TVPRM members that better represents the large regional decrease in ΔCO_2 observed on the North Slope (Fig. 3c).
356 While all coastal tundra sites respond similarly to T_s during the cold season, we determine that the CO_2 flux magnitude at
357 CMDL is most consistent with the regional observations (Fig. S11). T_s from ERA5 remain warmer throughout the late cold
358 season compared to those from NARR, which causes simulations using ERA5 T_s to overestimate CO_2 release during that time
359 (Fig. S11). Unlike during the growing season, cold season CO_2 fluxes are not sensitive to the vegetation distribution and SIF
360 products.

361 Finally, we identify the TVPRM member that best matches the observed ΔCO_2 : parameterized by IVO inland tundra
362 and CMDL coastal tundra site responses, distributed by the ABoVE LC vegetation map, and driven by NARR reanalysis and
363 the CSIF SIF product (referred to here as TVPRM Constrained, Figs. S6, S12). This constrained simulation estimates a mean
364 regional CO_2 flux of $0.05 \mu\text{mol m}^{-2} \text{s}^{-1}$ for the late cold season in 2012–2015 and reproduces well the observed ΔCO_2 during
365 this time (Fig. 4a). The late cold season NMB and RMSE against the observations at the NOAA BRW tower are reduced from
366 4.91 to 2.04 and from 1.94 to 1.30, respectively, for the constrained simulation compared to the median of the entire TVPRM
367 ensemble (Fig. S12). However, the early cold season CO_2 emissions, with a mean regional CO_2 flux of $0.25 \mu\text{mol m}^{-2} \text{s}^{-1}$ for
368 September–December (Fig. S13a), are still underestimated, with the simulated ΔCO_2 lower than the observed ΔCO_2 by ~ 5
369 ppm (Fig. 4a).

370 **3.2 Alternative T_s products and R_{soil} parameterizations**

371 To test the impact of reanalysis T_s on the early cold season CO_2 fluxes, we implement T_s that are more specifically developed
372 to represent Alaska tundra permafrost soils during freeze-thaw processes than the reanalysis products driving our constrained
373 TPVRM member. A single layer of T_s at 8 cm depth from RS-PM (Fig. S14a) captures the magnitude and temporal behavior
374 of the observed early cold season CO_2 fluxes slightly better than the constrained member (Figs. 4a, S12), which uses NARR
375 reanalysis T_s and does not incorporate permafrost-model derived T_s . The RS-PM T_s extends CO_2 emission fluxes further into
376 the cold season by up to a month, which is consistent with a better representation of the zero-curtain period, however, emissions
377 remain higher throughout the late cold season than our atmospheric observation-constrained CO_2 fluxes (Fig. S15). We also
378 test the implementation of a multi-layer fit driven by soil column temperature from RS-PM, but neither of these instances of
379 remote sensing informed T_s substantially improve the agreement of the ΔCO_2 at the NOAA BRW tower during the early cold

380 season. Attempts to use alternative R_{soil} formulations based on T_s , including Q_{10} relationships, also fail to reproduce the
 381 observed elevated CO_2 fluxes during the cold season.



382
 383 **Figure 4.** Tall tower atmospheric observations of the Alaska North Slope support early cold season emissions not driven by soil temperature
 384 (T_s) and present no evidence for elevated late cold season emissions. (a)–(b) Comparison of hourly cold season (Sep–Apr) observed and
 385 simulated ΔCO_2 at the NOAA BRW tower for the constrained TPVRM member, where soil respiration (R_{soil}) is determined only by T_s (a)
 386 and for the constrained TVPRM member + additional zero-curtain emissions (ZC) and inland water fluxes (IW) (b). Horizontal segments
 387 indicate range of uncertainty in the NOAA BRW tower ocean sector background calculation. Shown with slope determined by ordinary least
 388 squares and coefficient of determination (R^2) of all points ($n = 191$). 1:1 line shown in dark gray. (c) Monthly cold season total Alaska North
 389 Slope net CO_2 fluxes for various CO_2 flux models. TVPRM-based simulations and Natali and Watts et al. (2019) show values for 2012–
 390 2017, Luus et al. (2017) show 2012–2014, and Watts et al. (2021) show Sep 2016–Apr 2017. Ribbons represent range of all years, where
 391 applicable. Area of the North Slope domain used to calculate regional totals is $3.537 \times 10^5 \text{ km}^2$.

392 3.3 Evaluation of other CO_2 flux models during the cold season

393 More early cold season (September–December) CO_2 flux into the atmosphere is observed at the NOAA BRW tower than is
 394 emitted by our constrained empirical simulation member, and these observations also indicate low late cold season (January–
 395 April) CO_2 emissions. We compare our constrained CO_2 fluxes to several other representations of gridded CO_2 flux on the
 396 North Slope (Table S3) and find that difficulty in simulating the magnitude and timing of the observed ΔCO_2 throughout the
 397 cold season is not unique to the constrained fluxes from our study.

398 The net CO₂ fluxes from Luus et al. (2017) are similar to the constrained TVPRM member during the growing season
399 (Fig. S16), but release more than three times as much CO₂ into the atmosphere throughout the late cold season (Fig. 4c). This
400 large late cold season CO₂ flux leads to a large overestimate compared to the observed ΔCO₂ (Fig. S14b). The optimization
401 employed by Commane et al. (2017) increases the September–October CO₂ flux to a range that matches our observations at
402 the NOAA BRW tower. However, Commane et al. (2017) did not optimize the cold season fluxes from November to March,
403 but reverted to Luus et al. (2017) fluxes during this time, thus producing late cold season fluxes that are too large. Overall,
404 Commane et al. (2017) projected a regional total cold season CO₂ source of 37–40 TgC for 2012–2014, which is more than
405 twice as high as our constrained TVPRM member CO₂ flux (15–18 TgC) for those years.

406 Carbon dioxide fluxes from work by Natali and Watts et al. (2019), a cold season model developed for the global
407 high latitude permafrost region, are similar to our constrained TVPRM member in September, but the fluxes remain high
408 throughout the cold season (Fig. 4c) similarly to Luus et al. (2017), for a range of total cold season CO₂ flux of 40–43 TgC for
409 2012–2017. This sustained CO₂ release also leads to an overestimation in the ΔCO₂ in the late cold season for this region (Fig.
410 S14c). Tao et al. (2021) also show that the cold season CO₂ fluxes of Natali and Watts et al. (2019) are high compared to their
411 model. More recent work by Watts et al. (2021), using observations from new Soil Respiration Station monitoring sites in
412 Alaska, produces cold season CO₂ fluxes more similar to our constrained CO₂ fluxes, with an underestimate in the simulated
413 ΔCO₂ during the early cold season (Fig. S14d), for a total cold season CO₂ flux of 18 TgC for September 2016 to April 2017.

414 **3.4 Sources of missing CO₂ fluxes**

415 None of the flux products discussed above, including our TVPRM ensemble, account for any potential CO₂ fluxes during the
416 zero-curtain period that are not driven by T_s or are from areas on the terrestrial-aquatic interface. To account for these processes,
417 we first add an additional CO₂ flux with zero-curtain timing to our constrained CO₂ flux (TVPRM) member from both inland
418 and coastal tundra areas that consists of 0.25 μmol m⁻² s⁻¹ for October with a reduction to zero by the end of December. This
419 peak additional CO₂ flux is within the daily variability of the observed CO₂ flux at the IVO and CMDL eddy flux sites during
420 the zero-curtain period (Fig. S9) and the reduction into December is consistent with these observations. The additional zero-
421 curtain flux improves the ability of the model to reproduce the observed ΔCO₂ at the NOAA BRW tower (slope = 0.46, R² =
422 0.41). We also apply the coastal tundra site ecosystem parameterization used in our constrained TVPRM member to all areas
423 of inland water on the North Slope, which account for 4% of the domain according to the ABoVE LC map (Fig. S5) and were
424 previously set to zero CO₂ flux. Representing these aquatic areas with biogenic CO₂ fluxes consistent with coastal tundra
425 ecosystems is one simple way to bridge the terrestrial-aquatic gap in tundra ecosystem models, where portions of aquatic
426 systems on the land-water gradient (i.e., the edges) may be more likely to respond to the environment as coastal tundra than
427 with the zero-flux assumed by water area. The ice phenology for areas of inland water producing CO₂ flux is then considered
428 to be similar to that of the freeze-thaw timing in coastal tundra soils. Adding these coastal tundra fluxes to inland water areas
429 also improves the performance of our model (slope = 0.32, R² = 0.30 against NOAA BRW tower observations). The magnitude

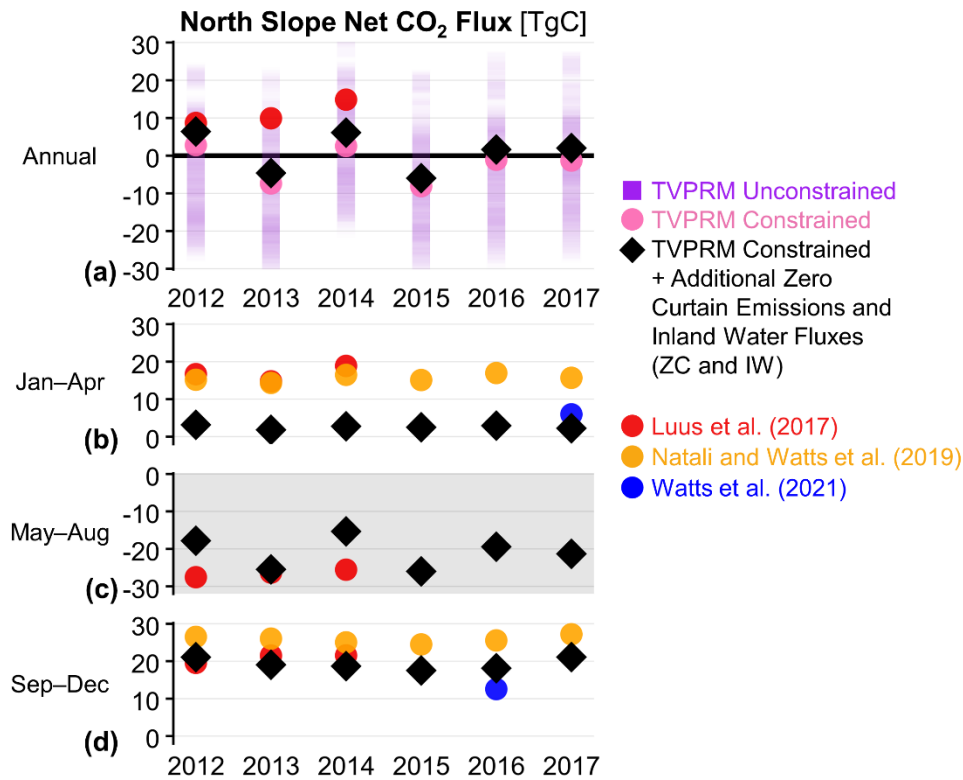
430 of additional zero-curtain flux suggested here and the portion of inland water represented with coastal tundra site
431 parameterizations produce the best statistical comparison for a range of choices tested (Fig. S17).

432 Together, adding these zero-curtain (ZC) and inland water (IW) CO₂ fluxes to our constrained simulation (referred to
433 as TVPRM Constrained + ZC and IW) increases the mean regional CO₂ flux in early cold season by 70% (0.18 μmol m⁻² s⁻¹,
434 Fig. S13b) and results in a large improvement to our comparison of ΔCO₂ at the NOAA BRW tower (slope = 0.54, R² = 0.40,
435 Figs. 4b, S12) and across the region using airborne data, especially during the November ABoVE Arctic-CAP flights (Figs. 2,
436 S6). The year-round comparison using all available aircraft and tower observations shows these net CO₂ fluxes are now
437 representative of the region (slope = 0.90, R² = 0.80, Fig. 2d). As a result, the North Slope regional total cold season CO₂ flux
438 increases by 6 TgC (~38%) to 20–24 TgC for 2012–2017 compared to the constrained empirical CO₂ flux model member.

439 **3.5 Alaska North Slope annual net CO₂ flux**

440 The median Alaska North Slope annual net CO₂ flux from the TVPRM ensemble (–5 TgC yr⁻¹) for 2012–2017 is consistent
441 with the previous multi-model comparison (Fisher et al., 2014), but we find a much smaller range in regional CO₂ flux values
442 (26 TgC yr⁻¹ to –29 TgC yr⁻¹ for 95% of TVPRM members) (Fig. S18). The largest contribution to this ensemble range comes
443 from the difference in parameterizations determined for the ICS and ICT inland tundra sites, with TVPRM members using ICS
444 trending toward a net CO₂ source, while ICT trends toward net CO₂ uptake. The distribution of inland and coastal tundra
445 throughout the region represented by the vegetation maps also has a noticeable impact on the sign of the net CO₂ flux, with
446 members using the RasterCAVM more likely to release net CO₂ into the atmosphere than members using the other maps.
447 There is also little interannual variability in the unconstrained TVPRM ensemble, with only 2014 moving toward a net CO₂
448 source, consistent with Tao et al. (2021) for these years.

449 Our best quantification of the annual net CO₂ flux for the North Slope informed by atmospheric observations, TVPRM
450 Constrained + ZC and IW, indicates that the region is a small net sink for 2013 (–5 TgC yr⁻¹) and 2015 (–6 TgC yr⁻¹) and a
451 small net source for 2012 (+6 TgC yr⁻¹), 2014 (+6 TgC yr⁻¹), 2016 (+2 TgC yr⁻¹), and 2017 (+2 TgC yr⁻¹) (Fig. 5a). We
452 estimate a 10% uncertainty in the net annual CO₂ flux based on the slope from our final comparison with the year-round
453 observations (Fig. 2d). The year-round net CO₂ fluxes from Luus et al. (2017) (driven with NARR meteorology, monthly
454 GOME-2 SIF, and CAVM vegetation map) indicate the North Slope to be a strong annual net CO₂ source for 2012–2014 (+9
455 TgC yr⁻¹ to +15 TgC yr⁻¹, Fig. S18) and are inconsistent with our results. Our results are more consistent with Tao et al. (2021),
456 but we find a smaller range in the magnitude of net CO₂ flux over the same years and more years trending toward a net CO₂
457 source.



458

459 **Figure 5.** Annual and seasonal Alaska North Slope net CO₂ flux constrained by aircraft and tower observations. (a) Annual, (b) late cold
460 season (Jan–Apr), (c) growing season (May–Aug), and (d) early cold season (Sep–Dec) total Alaska North Slope net CO₂ fluxes for various
461 CO₂ flux models for 2012–2017 as in Fig. 4. Purple squares indicate middle 95% of all TVPRM ensemble members.

462 We find that the regional net growing season CO₂ uptake and the cold season emissions on the North Slope are
463 comparable in magnitude, so the net balance could depend on small perturbations in either flux. However, the regional cold
464 season CO₂ emissions for these years were relatively similar from year to year: 18–21 TgC for the early cold season (Fig. 5d),
465 diminishing to only 2–3 TgC for the late cold season (Fig. 5b). Therefore, the interannual variability of the regional carbon
466 balance is largely driven by fluctuating net growing season CO₂ fluxes during these years: greater net growing season uptake
467 in 2013 and 2015 than in 2012, 2014, 2016, and 2017 (Fig. 5c).

468 4. Discussion

469 4.1 Tundra ecosystem growing season net CO₂ fluxes

470 The good performance of the TVPRM ensemble against the atmospheric observations during the growing season indicates that
471 the tundra ecosystems of the Alaska North Slope respond to light and heat as quantified by PAR, T_s, and T_a, and that the net
472 CO₂ flux is largely controlled by the simple R_{soil}, R_{plant}, and GPP relationships in the empirical model over this time.

473 The growing season of each year determines the sign of the regional annual net CO₂ flux during our study period,
474 with 2013 and 2015 being strong net sinks and 2014 being the strongest net source. The relative magnitude of each component
475 of the net CO₂ flux during the growing season (i.e., R_{soil}, R_{plant}, GPP) varies from year-to-year (Table S7) and helps explain the
476 interannual variability in the net source or sink status of the North Slope. Growing season 2015 was very warm, dry, and sunny
477 in Alaska and resulted in extreme biomass burning activity outside of the North Slope (Table S1). High regional mean T_a and
478 PAR (Table S8) and low accumulated precipitation (Table S9) in NARR confirm this was the case for North Slope as well,
479 with high T_a and PAR contributing to a very high GPP. The growing season SIF signal from the CSIF product, which
480 determines the seasonal cycle and relative magnitude of photosynthetic activity, is also large in 2015 (Table S8), further
481 enhancing GPP. This year and others with a larger GPP component of NEE correspond to growing seasons with stronger SIF
482 signals, which is an indicator of increased productivity and consistent with previous studies (e.g., Magney et al., 2019; Sun et
483 al., 2017). While fairly high T_a and T_s in 2015 also result in high R_{soil} and R_{plant}, respectively, this elevated respiration is not
484 enough to offset the very high GPP and results in a large net CO₂ sink. In contrast, the summer of 2014 was cool, wet, and
485 cloudy, and the North Slope experienced very low T_a, PAR, and SIF signal, producing very low GPP. Lower-than-normal T_a
486 also results in very low R_{plant}, but as with 2015, this is not enough to offset the extremely low uptake resulting in a large net
487 CO₂ source for 2014. In 2013, the other growing season with a strong net CO₂ sink, moderately high GPP combines with
488 moderately low R_{plant} and very low R_{soil}. Extremely low T_s causes this very low R_{soil}, which, relative to moderate T_a and PAR,
489 is likely a result of above-average lingering snowpack into May (Table S9). This lingering snowpack is perhaps surprising
490 given that the mean snowpack for the proceeding cold season was not particularly deep. The important impact that snow cover
491 and the timing of snowmelt has on T_s and carbon response in tundra ecosystems has been recently emphasized (e.g., Kim et
492 al., 2021), and is supported by our work, which shows that the prevalence of snow in the spring may determine the sign of the
493 regional net CO₂ for an entire year.

494 The regional net CO₂ flux is highly sensitive, however, to the distribution of tundra vegetation types (upland v.
495 coastal) throughout the North Slope during the growing season. Coastal tundra takes up more CO₂ for a given unit PAR
496 compared to inland tundra, based on the relationships between observed site-level net CO₂ flux and PAR in this study (TVPRM
497 parameters, Fig. S1), which could be evidence for an adaptation to lower light levels. This difference is consistent with Luus
498 et al. (2017), who calculated greater uptake at “wetland” sites like Atqasuk and Barrow than at “graminoid tundra” sites like
499 Ivotuk and Imnavait when all driver inputs are constant and with Mbufong et al. (2014), who also found that peak growing
500 season net uptake for constant light is greater at Barrow than at Ivotuk. The stronger CO₂ uptake response of coastal tundra to
501 light is important to consider due to the fact that the vegetation distributions assessed here with more coastal tundra to the
502 south (CAVM (Walker et al., 2005), ABoVE LC (Wang et al., 2020)) better agree with the atmospheric observations. When
503 considering the ability of coastal tundra to take up CO₂ when moved toward the south, Patankar et al. (2013) saw that tundra
504 plants exposed to additional intense light did not respond with additional uptake. Therefore, while the ecosystem response of
505 the southern North Slope is more consistent with coastal ecosystems, it seems possible that these areas are misclassified in
506 either our simplified two-tundra type scheme or in the vegetation maps themselves. The large variability in net CO₂ flux

507 calculated by using the different maps supports the importance of accurate ecosystem type locations in upscaling eddy flux
508 measurements and highlights the need for improved vegetation mapping and classification schemes in the Arctic ecology
509 research community.

510 **4.2 Regional-scale cold season CO₂ emissions**

511 Observations across scales, at the in-situ eddy flux towers, the NOAA BRW tower, and from aircraft, consistently show signs
512 of large early cold season CO₂ emissions from ecosystems on the Alaska North Slope. However, there is no evidence of
513 widespread elevated emissions in this region during the late cold season, contrary to other studies (Commane et al., 2017;
514 Natali and Watts et al., 2019). The TVPRM ensemble parameterizations using terrestrial eddy flux sites and the fluxes from
515 other terrestrial CO₂ models cannot reproduce both the observed magnitude and across-season timing of these cold season CO₂
516 emissions.

517 The largest differences in the net CO₂ flux between TVPRM ensemble members result from the contrasting site conditions
518 driving the ICS and ICT R_{soil} parameterizations during the cold season. When taken separately by cold season segment, ICS
519 members perform quite well against observations at the NOAA BRW tower for early cold season and ICT members perform
520 well for the late cold season. The contrasting performance between site parameterizations is due to the topographic and
521 hydrologic conditions, which are quite heterogeneous over a short distance and influence the plant communities and carbon
522 storage, at each site. The ecosystems sampled by the ICS tower are seasonally inundated and retain a deep layer of organic soil
523 that can be respired in greater amounts longer into the early cold season, while the well-drained hillslope at ICT does not allow
524 for accumulation of organic matter in the same way (Euskirchen et al., 2017; Larson et al., 2021). While varying topography
525 and soil inundation throughout the North Slope means that each of these site relationships is likely to be representative of many
526 other locations in the region with similar conditions, the early-to-late cold season reduction in CO₂ fluxes at these sites is not
527 consistent with the observed regional atmospheric trend, however, and we remove the members parameterized by them from
528 the ensemble. Individual eddy flux site parameterizations may reproduce regional CO₂ fluxes for a given season, but it is
529 important to consider their response to drivers across multiple seasons when scaling from the site-level to regional domains.

530 The observed cold season CO₂ flux pattern on the North Slope may be unique to tundra ecosystems of this region. For
531 example, the CO₂ fluxes from Natali and Watts et al. (2019) and Watts et al. (2021) both incorporate measurements from the
532 North Slope. However, Natali and Watts et al. (2019) used boosted regression trees trained on belowground respiration
533 measurements from across the pan-Arctic tundra and boreal zones, which may not be representative for our study region. The
534 fluxes from Watts et al. (2021) are based on respiration measurements from throughout only Alaska and northwest Canada
535 and conform better to local conditions. The evaluation of these CO₂ fluxes against atmospheric CO₂ measurements also
536 produces results that are more consistent with our TVPRM ensemble determined by North Slope eddy flux tower
537 measurements.

538 We find that the atmospheric observations are best matched by biogenic CO₂ fluxes that include an additional CO₂ source
539 from tundra ecosystems during the zero-curtain period that are independent from T_s variability and year-round net CO₂ fluxes

540 from areas of inland water. The additional zero-curtain flux represents large-scale emission events not directly timed to
541 microbial activity and root respiration controlled by T_s , but could be related to the delayed physical release of previously
542 produced CO_2 from soil through the snowpack as the soil layers remain unfrozen (Bowling and Massman, 2011). The Alaska
543 North Slope also has many water bodies distributed throughout the coastal tundra region, and the extent to which carbon cycles
544 between small, shallow ponds and their surrounding terrestrial components is unclear (Magnússon et al., 2020). The biogenic
545 CO_2 fluxes in these areas are likely driven by ecosystem-scale CO_2 fluxes from both coastal tundra and small ponds (Holgerson
546 and Raymond, 2016; Tan et al., 2017) and their impact on the regional net CO_2 flux, via both emissions and uptake, may be
547 significant (Elder et al., 2018; Beckebanze et al., 2022). Only by adding fluxes that match observed zero-curtain CO_2 emission
548 pulses and by approximating net CO_2 fluxes in aquatic areas can we reproduce the observed ΔCO_2 magnitude in both early
549 and late cold season. The resulting seasonal change between the early and late cold season is consistent with the extended
550 duration of the observed regional-scale zero curtain. The simplistic approximations suggested here are not inconsistent with
551 the existing uncertainties in tundra CO_2 flux modeling and demonstrate the importance of considering these additional CO_2
552 fluxes and their mechanisms for future study.

553 **4.3 Future state of net CO_2 flux on the Alaska North Slope**

554 As the Arctic warms rapidly, the competition between the growing and cold season Arctic CO_2 fluxes will determine the net
555 biogenic CO_2 flux into the atmosphere. Warming T_a warms soils, thaws permafrost, increases active layer thickness and has
556 extended the duration of the zero curtain from weeks to over 100 days (Romanovsky and Osterkamp, 2000; Schuur et al.,
557 2015; Zona et al., 2016), all of which increase cold season CO_2 emissions. The warming may also increase net growing season
558 uptake, but the severe light limitation at high northern latitudes limits the extent of the growing season, especially on the North
559 Slope (Zhang et al., 2020). The future of CO_2 fluxes from inland waters and wetlands in the Arctic is uncertain, but some
560 studies suggest CO_2 emissions from lakes may increase (Bayer et al., 2019). The culmination of these effects will likely push
561 the North Slope into a consistent net source in the future. However, observations at the NOAA BRW tower during our study
562 period do not show elevated late cold season CO_2 emissions, so the North Slope was not a consistent net source through 2017.
563 Accordingly, care must be taken to accurately represent CO_2 fluxes from Arctic ecosystems during both the early and late cold
564 season when calculating the annual net CO_2 budget. TVPRM could be used with projections of meteorology and SIF to
565 calculate the future net CO_2 balance for this region, but we caution against overuse of the model using current parameters, as
566 the flux-driver relationships in the rapidly warming Arctic ecosystems are changing so quickly that we would not assume
567 accuracy into the future. While we can constrain the annual net CO_2 budget with existing data, the Arctic is rapidly changing
568 and needs constant monitoring. The following recommendations would provide more detailed spatial and seasonal constraints
569 and up-to-date information on the processes driving CO_2 fluxes across the region.

570 **4.3.1 Future observation efforts**

571 Our results motivate the need for a more extensive network of CO₂ eddy flux towers operating year-round, alongside sensors
572 for soil moisture and T_s profiles throughout the active layer to better understand the mechanisms driving year-round and
573 especially early cold season CO₂ fluxes. Noting that automated or semi-automated monitoring systems for aquatic
574 environments currently do not exist for the North Slope or other high latitude regions, this sensor network should be distributed
575 throughout poorly sampled ecosystem types, particularly along wetness gradients that span mixed terrestrial-aquatic
576 environments. The results in this study also support the need for additional continuous CO₂ concentration measurements at tall
577 towers across the North Slope (including away from the coast) to increase coverage of observed ΔCO₂ during all seasons and
578 to better constrain the regional background. Airborne measurements of both CO₂ concentrations and CO₂ fluxes remain
579 valuable to sample areas less accessible via ground-based measurements, but a large-scale flight campaign in the region has
580 not occurred since 2017. Any additional flights should be targeted as early before, and as late after, the growing season as
581 possible. Satellites that rely on reflected sunlight to detect CO₂ have increasingly been used to constrain CO₂ budgets in the
582 northern latitudes (e.g., Byrne et al., (2022)), but data is very limited in the cold season, especially in far-northern regions like
583 the North Slope.

584 **4.3.2 Future modeling efforts**

585 The large initial range of potential regional net CO₂ flux values we found for the Alaska North Slope indicates a large sensitivity
586 to choices and assumptions made when scaling eddy flux observations from the site- to regional- scale. The most important of
587 these choices are the representation of the upland tundra, particularly for the response of R_{soil} to T_s during the cold season, and
588 the distribution of vegetation types throughout the domain. Future tundra CO₂ modeling efforts should focus on using site-
589 level data that is the most consistent with regional-scale fluxes, rather than incorporating data from all available sites.
590 Consistency and accuracy in classification schemes used in vegetation maps must also be addressed. As we have shown with
591 the atmospheric observations, not all model scenarios have equal likelihood to be true, and the mean of the model ensemble is
592 not necessarily the most likely or most consistent with the atmosphere. Using these atmospheric observations is uncertain,
593 however, due to potential errors in the transport modeling, which are difficult to quantify. Atmospheric modeling of remote
594 areas such as the Alaska North Slope requires further evaluation and improvement. Further, increasing model temporal
595 resolution should be considered as the importance of the zero-curtain and snow cover to the net CO₂ flux of tundra ecosystems
596 is recognized, both of which vary on the order of days and weeks, rather than months.

597 **5. Conclusions**

598 Observed atmospheric concentrations from aircraft and towers are a powerful tool that provide a regional constraint on the
599 many combinations of possible CO₂ flux parameterizations and distributions of tundra ecosystems on the North Slope of
600 Alaska. We find that the annual regional net CO₂ flux on the North Slope is not a consistent net source or sink, but instead

601 varies between -6 and $+6$ TgC yr⁻¹ for 2012–2017. We can also identify ecosystem relationships and driver combinations that
602 best represent both local CO₂ flux patterns and regional atmospheric CO₂ enhancements. The simulated regional net CO₂ flux
603 is highly sensitive to assumptions made while scaling up eddy flux observations, especially the ecosystem response to T_s of
604 tundra during the cold season and the spatial distribution of tundra types across the North Slope. Additionally, scaling methods
605 that average observations from multiple eddy covariance flux sites should consider which sites are most representative of the
606 regional impact of the biosphere on the atmosphere using integrative top-down observations.

607 This work shows that year-round measurements of atmospheric CO₂ concentrations and fluxes across heterogeneous
608 terrestrial and aquatic ecosystems are needed to represent the drivers of CO₂ fluxes from Arctic regions. Arctic ecosystems
609 have the potential to accelerate warming if vast stores of carbon are released or buffer warming if increasing carbon uptake
610 from vegetation occurs. All components of Arctic tundra ecosystems must be fully incorporated into earth system models to
611 improve projections of future climate warming and associated carbon cycle feedbacks.

612 **Data availability**

613 Data that support the findings of this study are available as listed below:

614 TVPRM NEE for all ensemble simulations: <https://doi.org/10.3334/ORNLDAAAC/1920>.

615 ICS, ICT, and ICH eddy flux tower observations: <http://aon.iab.uaf.edu/data>.

616 IVO, ATQ, BES, BEO, and CMDL eddy flux tower observations: <https://doi.org/10.18739/A2X34MS1B>.

617 NOAA BRW tower observations: <https://www.esrl.noaa.gov/gmd/dv/data/?site=brw>.

618 ARM-ACME V aircraft observations: <https://www.osti.gov/dataexplorer/biblio/dataset/1346549>.

619 ABoVE Arctic-CAP aircraft observations: <https://doi.org/10.3334/ORNLDAAAC/1658>.

620 NARR meteorology: <https://psl.noaa.gov/data/gridded/data.narr.html>.

621 ERA5 meteorology: <https://www.ecmwf.int/en/forecasts/dataset/ecmwf-reanalysis-v5>.

622 GOME-2 SIF: https://avdc.gsfc.nasa.gov/pub/data/satellite/MetOp/GOME_F/.

623 GOSIF: <https://globalecology.unh.edu/data/GOSIF.html>.

624 CSIF: <http://doi.org/10.6084/m9.figshare.6387494>.

625 CAVM vegetation map: <https://www.geobotany.uaf.edu/cavm/>.

626 RasterCAVM vegetation map: <https://dx.doi.org/10.17632/c4xj5rv6kv.1>.

627 ABoVE LC vegetation map: <https://doi.org/10.3334/ORNLDAAAC/1691>.

628 RS-PM T_s: available from authors upon request.

629 NOAA BRW tower and ARM-ACME V aircraft campaign WRF-STILT footprints:

630 <https://doi.org/10.3334/ORNLDAAAC/1431>, particle trajectories: <https://doi.org/10.3334/ORNLDAAAC/1430>.

631 ABoVE Arctic-CAP aircraft campaign WRF-STILT footprints: <https://doi.org/10.3334/ORNLDAAAC/1896>, particle

632 trajectories: <https://doi.org/10.3334/ORNLDAAAC/1895>.

- 633 Luus et al. (2017) fluxes: <https://doi.org/10.3334/ORNLDAAAC/1314>.
634 Commane et al. (2017) optimized fluxes: <https://doi.org/10.3334/ORNLDAAAC/1389>.
635 Natali and Watts et al. (2019) fluxes: <https://doi.org/10.3334/ORNLDAAAC/1683>.
636 Watts et al. (2021) fluxes: <https://doi.org/10.3334/ORNLDAAAC/1935>.

637 **Author contributions**

638 LDS and RC designed the study. KAA, ESE, JPG, AK, WCO, and DZ provided eddy covariance flux tower data. SCB, KM,
639 and CS provided aircraft concentration data. JMH and MEM provided WRF-STILT particle files and footprints. YY provided
640 RS-PM T_s data. JDW provided Watts et al. (2021) cold season belowground CO₂ fluxes. LDS developed and evaluated
641 TVPRM net CO₂ fluxes against observations. RC, EJLL, JWM, and JDW assisted the analysis. LDS wrote the paper. All co-
642 authors contributed to the preparation of the manuscript.

643 **Competing interests**

644 Authors declare that they have no competing interests.

645 **Acknowledgments**

646 We would like to acknowledge that the Alaskan North Slope is home to multiple Alaska Native nations, including the
647 Nunamiut, Gwich'in, Koyukuk, and Iñupiaq peoples. We support and honor the place-based knowledge of Indigenous Peoples
648 and recognize their ancestral and contemporary stewardship of their homelands that we research. LDS and RC are supported
649 by research funding from the Department of Earth and Environmental Sciences at Columbia University and the NASA ABoVE
650 grant #NNX17AC61A. LDS is additionally supported by the National Science Foundation (NSF) Office of Polar Programs
651 grant #1848620. EJRL and JWM are supported by NASA ABoVE grant #NNX17AE75G. JDW is supported by NASA
652 ABoVE grant #80NSSC19M0209 and NASA grant #NNH17ZDA001N-NIP. Part of the research was carried out at the Jet
653 Propulsion Laboratory, California Institute of Technology, under a contract with NASA (80NM0018D0004). Imnavait Creek
654 flux towers are funded under grants from the NSF Office of Polar Programs, 1503912 and 0632264. Resources supporting
655 JMH and WRF-STILT modeling were provided by NASA grant #NNX17AE75G, #NNX17AC61A, and the NASA High-End
656 Computing (HEC) Program through the NASA Advanced Supercomputing (NAS) Division at Ames Research Center. We
657 thank the R Project community for analysis and plotting tools, especially the ggplot2, ggpattern, magick, anytime, lubridate,
658 raster, and cowplot packages. NCEP Reanalysis data provided by the NOAA/OAR/ESRL PSL, Boulder, Colorado, USA.
659 Some of the data products used in this paper were acquired for the CARVE, a NASA Earth Ventures Sub-orbital (EV-S1)
660 investigation.

661 **References**

- 662 Arndt, K. A., Oechel, W. C., Goodrich, J. P., Bailey, B. A., Kalhori, A., Hashemi, J., Sweeney, C., and Zona, D.: Sensitivity
663 of Methane Emissions to Later Soil Freezing in Arctic Tundra Ecosystems, *J. Geophys. Res. Biogeosci.*, 124, 2595–2609,
664 <https://doi.org/10.1029/2019JG005242>, 2019.
- 665 Arndt, K. A., Lipson, D. A., Hashemi, J., Oechel, W. C., and Zona, D.: Snow melt stimulates ecosystem respiration in Arctic
666 ecosystems, *Global Change Biol.*, 26, 5042–5051, <https://doi.org/10.1111/gcb.15193>, 2020.
- 667 Bayer, T. K., Gustafsson, E., Brakebusch, M., and Beer, C.: Future Carbon Emission From Boreal and Permafrost Lakes Are
668 Sensitive to Catchment Organic Carbon Loads, *J. Geophys. Res. Biogeosci.*, 124, 1827–1848,
669 <https://doi.org/10.1029/2018JG004978>, 2019.
- 670 Beckebanze, L., Rehder, Z., Holl, D., Wille, C., Mirbach, C., and Kutzbach, L.: Ignoring carbon emissions from thermokarst
671 ponds results in overestimation of tundra net carbon uptake, *Biogeosciences*, 19, 1225–1244, <https://doi.org/10.5194/bg-19-1225-2022>, 2022.
- 673 Biraud, S., Mei, F., Flynn, C., Hubbe, J., Long, C., Matthews, A., Pekour, M., Sedlacek, A., Springston, S., Tomlinson, J., and
674 Chand, D.: Campaign datasets for ARM Airborne Carbon Measurements (ARM-ACME-V), Oak Ridge National Lab.
675 (ORNL), Oak Ridge, TN (United States). Atmospheric Radiation Measurement (ARM) Archive,
676 <https://doi.org/10.5439/1346549>, 2016.
- 677 Bowling, D. R. and Massman, W. J.: Persistent wind-induced enhancement of diffusive CO₂ transport in a mountain forest
678 snowpack, *J. Geophys. Res. Biogeosci.*, 116, G04006, <https://doi.org/10.1029/2011JG001722>, 2011.
- 679 Box, J. E., Colgan, W. T., Christensen, T. R., Schmidt, N. M., Lund, M., Parmentier, F.-J. W., Brown, R., Bhatt, U. S.,
680 Euskirchen, E. S., Romanovsky, V. E., Walsh, J. E., Overland, J. E., Wang, M., Corell, R. W., Meier, W. N., Wouters, B.,
681 Mernild, S., Maaß, J., Pawlak, J., and Olsen, M. S.: Key indicators of Arctic climate change: 1971–2017, *Environ. Res. Lett.*,
682 14, 045010, <https://doi.org/10.1088/1748-9326/aafc1b>, 2019.
- 683 Byrne, B., Liu, J., Yi, Y., Chatterjee, A., Basu, S., Cheng, R., Doughty, R., Chevallier, F., Bowman, K. W., Parazoo, N. C.,
684 Crisp, D., Li, X., Xiao, J., Sitch, S., Guenet, B., Deng, F., Johnson, M. S., Philip, S., McGuire, P. C., and Miller, C. E.: Multi-
685 year observations reveal a larger than expected autumn respiration signal across northeast Eurasia, *Biogeosciences*, 19, 4779–
686 4799, <https://doi.org/10.5194/bg-19-4779-2022>, 2022.
- 687 Chang, R. Y.-W., Miller, C. E., Dinardo, S. J., Karion, A., Sweeney, C., Daube, B. C., Henderson, J. M., Mountain, M. E.,
688 Eluszkiewicz, J., Miller, J. B., Bruhwiler, L. M. P., and Wofsy, S. C.: Methane emissions from Alaska in 2012 from CARVE
689 airborne observations, *PNAS*, 111, 16694–16699, <https://doi.org/10.1073/pnas.1412953111>, 2014.
- 690 Commane, R., Lindaas, J., Benmergui, J., Luus, K. A., Chang, R. Y.-W., Daube, B. C., Euskirchen, E. S., Henderson, J. M.,
691 Karion, A., Miller, J. B., Miller, S. M., Parazoo, N. C., Randerson, J. T., Sweeney, C., Tans, P., Thoning, K., Veraverbeke, S.,
692 Miller, C. E., and Wofsy, S. C.: Carbon dioxide sources from Alaska driven by increasing early winter respiration from Arctic
693 tundra, *PNAS*, 114, 5361–5366, <https://doi.org/10.1073/pnas.1618567114>, 2017.
- 694 Elder, C. D., Xu, X., Walker, J., Schnell, J. L., Hinkel, K. M., Townsend-Small, A., Arp, C. D., Pohlman, J. W., Gaglioti, B.
695 V., and Czimeczik, C. I.: Greenhouse gas emissions from diverse Arctic Alaskan lakes are dominated by young carbon, *Nature*
696 *Clim. Change*, 8, 166–171, <https://doi.org/10.1038/s41558-017-0066-9>, 2018.

- 697 Euskirchen, E. S., Bret-Harte, M. S., Scott, G. J., Edgar, C., and Shaver, G. R.: Seasonal patterns of carbon dioxide and water
698 fluxes in three representative tundra ecosystems in northern Alaska, *Ecosphere*, 3, art4, <https://doi.org/10.1890/ES11-00202.1>,
699 2012.
- 700 Euskirchen, E. S., Bret-Harte, M. S., Shaver, G. R., Edgar, C. W., and Romanovsky, V. E.: Long-Term Release of Carbon
701 Dioxide from Arctic Tundra Ecosystems in Alaska, *Ecosystems*, 20, 960–974, <https://doi.org/10.1007/s10021-016-0085-9>,
702 2017.
- 703 Fisher, J. B., Sikka, M., Oechel, W. C., Huntzinger, D. N., Melton, J. R., Koven, C. D., Ahlström, A., Arain, M. A., Baker, I.,
704 Chen, J. M., Ciais, P., Davidson, C., Dietze, M., El-Masri, B., Hayes, D., Huntingford, C., Jain, A. K., Levy, P. E., Lomas, M.
705 R., Poulter, B., Price, D., Sahoo, A. K., Schaefer, K., Tian, H., Tomelleri, E., Verbeeck, H., Viovy, N., Wania, R., Zeng, N.,
706 and Miller, C. E.: Carbon cycle uncertainty in the Alaskan Arctic, *Biogeosciences*, 11, 4271–4288, [https://doi.org/10.5194/bg-](https://doi.org/10.5194/bg-11-4271-2014)
707 11-4271-2014, 2014.
- 708 Goodrich, J. P., Oechel, W. C., Gioli, B., Moreaux, V., Murphy, P. C., Burba, G., and Zona, D.: Impact of different eddy
709 covariance sensors, site set-up, and maintenance on the annual balance of CO₂ and CH₄ in the harsh Arctic environment, *Agr.*
710 *Forest Meteorol.*, 228–229, 239–251, <https://doi.org/10.1016/j.agrformet.2016.07.008>, 2016.
- 711 Hartery, S., Commane, R., Lindaas, J., Sweeney, C., Henderson, J., Mountain, M., Steiner, N., McDonald, K., Dinardo, S. J.,
712 Miller, C. E., Wofsy, S. C., and Chang, R. Y.-W.: Estimating regional-scale methane flux and budgets using CARVE aircraft
713 measurements over Alaska, *Atmos. Chem. Phys.*, 18, 185–202, <https://doi.org/10.5194/acp-18-185-2018>, 2018.
- 714 Henderson, J. M., Eluszkiewicz, J., Mountain, M. E., Nehrkorn, T., Chang, R. Y.-W., Karion, A., Miller, J. B., Sweeney, C.,
715 Steiner, N., Wofsy, S. C., and Miller, C. E.: Atmospheric transport simulations in support of the Carbon in Arctic Reservoirs
716 Vulnerability Experiment (CARVE), *Atmos. Chem. Phys.*, 15, 4093–4116, <https://doi.org/10.5194/acp-15-4093-2015>, 2015.
- 717 Hersbach, H., Bell, B., Berrisford, P., Hirahara, S., Horányi, A., Muñoz-Sabater, J., Nicolas, J., Peubey, C., Radu, R., Schepers,
718 D., Simmons, A., Soci, C., Abdalla, S., Abellan, X., Balsamo, G., Bechtold, P., Biavati, G., Bidlot, J., Bonavita, M., Chiara,
719 G. D., Dahlgren, P., Dee, D., Diamantakis, M., Dragani, R., Flemming, J., Forbes, R., Fuentes, M., Geer, A., Haimberger, L.,
720 Healy, S., Hogan, R. J., Hólm, E., Janisková, M., Keeley, S., Laloyaux, P., Lopez, P., Lupu, C., Radnoti, G., Rosnay, P. de,
721 Rozum, I., Vamborg, F., Villaume, S., and Thépaut, J.-N.: The ERA5 global reanalysis, *Q. J. Roy. Meteorol. Soc.*, 146, 1999–
722 2049, <https://doi.org/10.1002/qj.3803>, 2020.
- 723 Holgerson, M. A. and Raymond, P. A.: Large contribution to inland water CO₂ and CH₄ emissions from very small ponds,
724 *Nat. Geosci.*, 9, 222–226, <https://doi.org/10.1038/ngeo2654>, 2016.
- 725 Hugelius, G., Strauss, J., Zubrzycki, S., Harden, J. W., Schuur, E. a. G., Ping, C.-L., Schirrmeister, L., Grosse, G., Michaelson,
726 G. J., Koven, C. D., O’Donnell, J. A., Elberling, B., Mishra, U., Camill, P., Yu, Z., Palmtag, J., and Kuhry, P.: Estimated stocks
727 of circumpolar permafrost carbon with quantified uncertainty ranges and identified data gaps, *Biogeosciences*, 11, 6573–6593,
728 <https://doi.org/10.5194/bg-11-6573-2014>, 2014.
- 729 Jeong, S.-J., Bloom, A. A., Schimel, D., Sweeney, C., Parazoo, N. C., Medvigy, D., Schaepman-Strub, G., Zheng, C., Schwalm,
730 C. R., Huntzinger, D. N., Michalak, A. M., and Miller, C. E.: Accelerating rates of Arctic carbon cycling revealed by long-
731 term atmospheric CO₂ measurements, *Sci. Adv.*, 4, eaao1167, <https://doi.org/10.1126/sciadv.aao1167>, 2018.
- 732 Joiner, J., Yoshida, Y., Guanter, L., and Middleton, E. M.: New methods for the retrieval of chlorophyll red fluorescence from
733 hyperspectral satellite instruments: simulations and application to GOME-2 and SCIAMACHY, *Atmos. Meas. Tech.*, 9, 3939–
734 3967, <https://doi.org/10.5194/amt-9-3939-2016>, 2016.

- 735 Karion, A., Sweeney, C., Kort, E. A., Shepson, P. B., Brewer, A., Cambaliza, M., Conley, S. A., Davis, K., Deng, A., Hardesty,
736 M., Herndon, S. C., Lauvaux, T., Lavoie, T., Lyon, D., Newberger, T., Pétron, G., Rella, C., Smith, M., Wolter, S., Yacovitch,
737 T. I., and Tans, P.: Aircraft-Based Estimate of Total Methane Emissions from the Barnett Shale Region, *Environ. Sci. Technol.*,
738 49, 8124–8131, <https://doi.org/10.1021/acs.est.5b00217>, 2015.
- 739 Kim, J., Kim, Y., Zona, D., Oechel, W., Park, S.-J., Lee, B.-Y., Yi, Y., Erb, A., and Schaaf, C. L.: Carbon response of tundra
740 ecosystems to advancing greenup and snowmelt in Alaska, *Nat. Commun.*, 12, 6879, [https://doi.org/10.1038/s41467-021-](https://doi.org/10.1038/s41467-021-26876-7)
741 26876-7, 2021.
- 742 Kim, Y., Kimball, J. S., Zhang, K., and McDonald, K. C.: Satellite detection of increasing Northern Hemisphere non-frozen
743 seasons from 1979 to 2008: Implications for regional vegetation growth, *Remote Sens. Environ.*, 121, 472–487,
744 <https://doi.org/10.1016/j.rse.2012.02.014>, 2012.
- 745 Kittler, F., Eugster, W., Foken, T., Heimann, M., Kolle, O., and Göckede, M.: High-quality eddy-covariance CO₂ budgets
746 under cold climate conditions, *J. Geophys. Res. Biogeosci.*, 122, 2064–2084, <https://doi.org/10.1002/2017JG003830>, 2017.
- 747 Larson, E. J. L., Schiferl, L. D., Commane, R., Munger, J. W., Trugman, A. T., Ise, T., Euskirchen, E. S., Wofsy, S., and
748 Moorcroft, P. M.: The changing carbon balance of tundra ecosystems: results from a vertically-resolved peatland biosphere
749 model, *Environ. Res. Lett.*, 17, 014019, <https://doi.org/10.1088/1748-9326/ac4070>, 2021.
- 750 Li, X. and Xiao, J.: A Global, 0.05-Degree Product of Solar-Induced Chlorophyll Fluorescence Derived from OCO-2, MODIS,
751 and Reanalysis Data, *Remote Sens.*, 11, 517, <https://doi.org/10.3390/rs11050517>, 2019.
- 752 Luus, K. A., Commane, R., Parazoo, N. C., Benmergui, J., Euskirchen, E. S., Frankenberg, C., Joiner, J., Lindaas, J., Miller,
753 C. E., Oechel, W. C., Zona, D., Wofsy, S., and Lin, J. C.: Tundra photosynthesis captured by satellite-observed solar-induced
754 chlorophyll fluorescence, *Geophys. Res. Lett.*, 44, 2016GL070842, <https://doi.org/10.1002/2016GL070842>, 2017.
- 755 Magney, T. S., Bowling, D. R., Logan, B. A., Grossmann, K., Stutz, J., Blanken, P. D., Burns, S. P., Cheng, R., Garcia, M. A.,
756 Köhler, P., Lopez, S., Parazoo, N. C., Raczka, B., Schimel, D., and Frankenberg, C.: Mechanistic evidence for tracking the
757 seasonality of photosynthesis with solar-induced fluorescence, *PNAS*, 116, 11640–11645,
758 <https://doi.org/10.1073/pnas.1900278116>, 2019.
- 759 Magnússon, R. Í., Limpens, J., van Huissteden, J., Kleijn, D., Maximov, T. C., Rotbarth, R., Sass-Klaassen, U., and Heijmans,
760 M. M. P. D.: Rapid Vegetation Succession and Coupled Permafrost Dynamics in Arctic Thaw Ponds in the Siberian Lowland
761 Tundra, *J. Geophys. Res. Biogeosci.*, 125, 2019JG005618, <https://doi.org/10.1029/2019JG005618>, 2020.
- 762 Mbufong, H. N., Lund, M., Aurela, M., Christensen, T. R., Eugster, W., Friborg, T., Hansen, B. U., Humphreys, E. R.,
763 Jackowicz-Korczynski, M., Kutzbach, L., Lafleur, P. M., Oechel, W. C., Parmentier, F. J. W., Rasse, D. P., Rocha, A. V.,
764 Sachs, T., van der Molen, M. K., and Tamstorf, M. P.: Assessing the spatial variability in peak season CO₂ exchange
765 characteristics across the Arctic tundra using a light response curve parameterization, *Biogeosciences*, 11, 4897–4912,
766 <https://doi.org/10.5194/bg-11-4897-2014>, 2014.
- 767 Meredith, M., Sommerkorn, M., Cassotta, S., Derksen, C., Ekaykin, A., Hollowed, A., Kofinas, G., Mackintosh, A.,
768 Melbourne-Thomas, J., Muelbert, M. M. C., Ottersen, G., Pritchard, H., and Schuur, E. A. G.: Polar Regions, in: IPCC Special
769 Report on the Ocean and Cryosphere in a Changing Climate, edited by: Pörtner, H.-O., Roberts, D. C., Masson-Delmotte, V.,
770 Zhai, P., Tignor, M., Poloczanska, E., Mintenbeck, K., Alegría, A., Nicolai, M., Okem, A., Petzold, J., Rama, B., and Weyer,
771 N. M., 2019.

- 772 Mesinger, F., DiMego, G., Kalnay, E., Mitchell, K., Shafran, P. C., Ebisuzaki, W., Jović, D., Woollen, J., Rogers, E., Berbery,
773 E. H., Ek, M. B., Fan, Y., Grumbine, R., Higgins, W., Li, H., Lin, Y., Manikin, G., Parrish, D., and Shi, W.: North American
774 Regional Reanalysis, *B. Am. Meteorol. Soc.*, 87, 343–360, <https://doi.org/10.1175/BAMS-87-3-343>, 2006.
- 775 Miller, S. M., Miller, C. E., Commane, R., Chang, R. Y.-W., Dinardo, S. J., Henderson, J. M., Karion, A., Lindaas, J., Melton,
776 J. R., Miller, J. B., Sweeney, C., Wofsy, S. C., and Michalak, A. M.: A multiyear estimate of methane fluxes in Alaska from
777 CARVE atmospheric observations, *Global Biogeochem. Cycles*, 30, 1441–1453, <https://doi.org/10.1002/2016GB005419>,
778 2016.
- 779 Natali, S. M., Watts, J. D., Rogers, B. M., Potter, S., Ludwig, S. M., Selbmann, A.-K., Sullivan, P. F., Abbott, B. W., Arndt,
780 K. A., Birch, L., Björkman, M. P., Bloom, A. A., Celis, G., Christensen, T. R., Christiansen, C. T., Commane, R., Cooper, E.
781 J., Crill, P., Czimeczik, C., Davydov, S., Du, J., Egan, J. E., Elberling, B., Euskirchen, E. S., Friborg, T., Genet, H., Göckede,
782 M., Goodrich, J. P., Grogan, P., Helbig, M., Jafarov, E. E., Jastrow, J. D., Kalhori, A. A. M., Kim, Y., Kimball, J. S., Kutzbach,
783 L., Lara, M. J., Larsen, K. S., Lee, B.-Y., Liu, Z., Lorant, M. M., Lund, M., Lupascu, M., Madani, N., Malhotra, A., Matamala,
784 R., McFarland, J., McGuire, A. D., Michelsen, A., Minions, C., Oechel, W. C., Olefeldt, D., Parmentier, F.-J. W., Pirk, N.,
785 Poulter, B., Quinton, W., Rezanezhad, F., Risk, D., Sachs, T., Schaefer, K., Schmidt, N. M., Schuur, E. A. G., Semenchuk, P.
786 R., Shaver, G., Sonntag, O., Starr, G., Treat, C. C., Waldrop, M. P., Wang, Y., Welker, J., Wille, C., Xu, X., Zhang, Z.,
787 Zhuang, Q., and Zona, D.: Large loss of CO₂ in winter observed across the northern permafrost region, *Nat. Clim. Change*,
788 9, 852–857, <https://doi.org/10.1038/s41558-019-0592-8>, 2019.
- 789 Oechel, W. C., Laskowski, C. A., Burba, G., Gioli, B., and Kalhori, A. A. M.: Annual patterns and budget of CO₂ flux in an
790 Arctic tussock tundra ecosystem, *J. Geophys. Res. Biogeosci.*, 119, 323–339, <https://doi.org/10.1002/2013JG002431>, 2014.
- 791 Outcalt, S. I., Nelson, F. E., and Hinkel, K. M.: The zero-curtain effect: Heat and mass transfer across an isothermal region in
792 freezing soil, *Water Resour. Res.*, 26, 1509–1516, <https://doi.org/10.1029/WR026i007p01509>, 1990.
- 793 Pallandt, M. M. T. A., Kumar, J., Mauritz, M., Schuur, E. A. G., Virkkala, A.-M., Celis, G., Hoffman, F. M., and Göckede,
794 M.: Representativeness assessment of the pan-Arctic eddy covariance site network and optimized future enhancements,
795 *Biogeosciences*, 19, 559–583, <https://doi.org/10.5194/bg-19-559-2022>, 2022.
- 796 Patankar, R., Mortazavi, B., Oberbauer, S. F., and Starr, G.: Diurnal patterns of gas-exchange and metabolic pools in tundra
797 plants during three phases of the arctic growing season, *Ecol. Evol.*, 3, 375–388, <https://doi.org/10.1002/ece3.467>, 2013.
- 798 Porcar-Castell, A., Tyystjärvi, E., Atherton, J., van der Tol, C., Flexas, J., Pfündel, E. E., Moreno, J., Frankenberg, C., and
799 Berry, J. A.: Linking chlorophyll a fluorescence to photosynthesis for remote sensing applications: mechanisms and challenges,
800 *J. Exp. Bot.*, 65, 4065–4095, <https://doi.org/10.1093/jxb/eru191>, 2014.
- 801 Reynolds, M. K., Walker, D. A., Balsler, A., Bay, C., Campbell, M., Cherosov, M. M., Daniëls, F. J. A., Eidesen, P. B.,
802 Ermokhina, K. A., Frost, G. V., Jedrzejek, B., Jorgenson, M. T., Kennedy, B. E., Kholod, S. S., Lavrinenko, I. A., Lavrinenko,
803 O. V., Magnússon, B., Matveyeva, N. V., Metúsalemsson, S., Nilsen, L., Olthof, I., Pospelov, I. N., Pospelova, E. B., Pouliot,
804 D., Razzhivin, V., Schaepman-Strub, G., Šibík, J., Telyatnikov, M. Yu., and Troeva, E.: A raster version of the Circumpolar
805 Arctic Vegetation Map (CAVM), *Remote Sens. Environ.*, 232, 111297, <https://doi.org/10.1016/j.rse.2019.111297>, 2019.
- 806 Romanovsky, V. E. and Osterkamp, T. E.: Effects of unfrozen water on heat and mass transport processes in the active layer
807 and permafrost, *Permafrost Periglac.*, 11, 219–239, [https://doi.org/10.1002/1099-1530\(200007/09\)11:3<219::AID-
808 PPP352>3.0.CO;2-7](https://doi.org/10.1002/1099-1530(200007/09)11:3<219::AID-PPP352>3.0.CO;2-7), 2000.
- 809 Schuur, E. A. G., McGuire, A. D., Schädel, C., Grosse, G., Harden, J. W., Hayes, D. J., Hugelius, G., Koven, C. D., Kuhry,
810 P., Lawrence, D. M., Natali, S. M., Olefeldt, D., Romanovsky, V. E., Schaefer, K., Turetsky, M. R., Treat, C. C., and Vonk, J.
811 E.: Climate change and the permafrost carbon feedback, *Nature*, 520, 171–179, <https://doi.org/10.1038/nature14338>, 2015.

- 812 Sun, Y., Frankenberg, C., Wood, J. D., Schimel, D. S., Jung, M., Guanter, L., Drewry, D. T., Verma, M., Porcar-Castell, A.,
813 Griffis, T. J., Gu, L., Magney, T. S., Köhler, P., Evans, B., and Yuen, K.: OCO-2 advances photosynthesis observation from
814 space via solar-induced chlorophyll fluorescence, *Science*, 358, eaam5747, <https://doi.org/10.1126/science.aam5747>, 2017.
- 815 Sweeney, C. and McKain, K.: ABoVE: Atmospheric Profiles of CO, CO₂ and CH₄ Concentrations from Arctic-CAP, 2017,
816 ORNL DAAC, <https://doi.org/10.3334/ORNLDAAC/1658>, 2019.
- 817 Sweeney, C., Dlugokencky, E., Miller, C. E., Wofsy, S., Karion, A., Dinardo, S., Chang, R. Y.-W., Miller, J. B., Bruhwiler,
818 L., Crotwell, A. M., Newberger, T., McKain, K., Stone, R. S., Wolter, S. E., Lang, P. E., and Tans, P.: No significant increase
819 in long-term CH₄ emissions on North Slope of Alaska despite significant increase in air temperature, *Geophys. Res. Lett.*, 43,
820 6604–6611, <https://doi.org/10.1002/2016GL069292>, 2016.
- 821 Sweeney, C., Chatterjee, A., Wolter, S., McKain, K., Bogue, R., Conley, S., Newberger, T., Hu, L., Ott, L., Poulter, B., Schiferl,
822 L., Weir, B., Zhang, Z., and Miller, C. E.: Using atmospheric trace gas vertical profiles to evaluate model fluxes: a case study
823 of Arctic-CAP observations and GEOS simulations for the ABoVE domain, *Atmos. Chem. Phys.*, 22, 6347–6364,
824 <https://doi.org/10.5194/acp-22-6347-2022>, 2022.
- 825 Tadić, J. M., Miller, S., Yadav, V., and Biraud, S. C.: Greenhouse gas fluxes from Alaska's North Slope inferred from the
826 Airborne Carbon Measurements Campaign (ACME-V), *Atmos. Environ.*, 118239,
827 <https://doi.org/10.1016/j.atmosenv.2021.118239>, 2021.
- 828 Tan, Z., Zhuang, Q., Shurpali, N. J., Marushchak, M. E., Biasi, C., Eugster, W., and Anthony, K. W.: Modeling CO₂ emissions
829 from Arctic lakes: Model development and site-level study, *J. Adv. Model. Earth Syst.*, 9, 2190–2213,
830 <https://doi.org/10.1002/2017MS001028>, 2017.
- 831 Tao, J., Zhu, Q., Riley, W. J., and Neumann, R. B.: Warm-season net CO₂ uptake
832 outweighs cold-season emissions over Alaskan North Slope tundra under current and RCP8.5 climate, *Environ. Res. Lett.*, 16,
833 055012, <https://doi.org/10.1088/1748-9326/abf6f5>, 2021.
- 834 Walker, D. A., Raynolds, M. K., Daniëls, F. J. A., Einarsson, E., Elvebakk, A., Gould, W. A., Katenin, A. E., Kholod, S. S.,
835 Markon, C. J., Melnikov, E. S., Moskalenko, N. G., Talbot, S. S., Yurtsev, B. A. (†), and Team, T. other members of the C.:
836 The Circumpolar Arctic vegetation map, *J. Veg. Sci.*, 16, 267–282, <https://doi.org/10.1111/j.1654-1103.2005.tb02365.x>, 2005.
- 837 Wang, J. A., Sulla-Menashe, D., Woodcock, C. E., Sonnentag, O., Keeling, R. F., and Friedl, M. A.: Extensive land cover
838 change across Arctic–Boreal Northwestern North America from disturbance and climate forcing, *Global Change Biol.*, 26,
839 807–822, <https://doi.org/10.1111/gcb.14804>, 2020.
- 840 Watts, J. D., Natali, S. M., Minions, C., Risk, D., Arndt, K., Zona, D., Euskirchen, E. S., Rocha, A. V., Sonnentag, O., Helbig,
841 M., Kalhori, A., Oechel, W., Ikawa, H., Ueyama, M., Suzuki, R., Kobayashi, H., Celis, G., Schuur, E. A. G., Humphreys, E.,
842 Kim, Y., Lee, B.-Y., Goetz, S., Madani, N., Schiferl, L. D., Commrane, R., Kimball, J. S., Liu, Z., Torn, M. S., Potter, S., Wang,
843 J. A., Jorgenson, M. T., Xiao, J., Li, X., and Edgar, C.: Soil respiration strongly offsets carbon uptake in Alaska and Northwest
844 Canada, *Environ. Res. Lett.*, 16, 084051, <https://doi.org/10.1088/1748-9326/ac1222>, 2021.
- 845 Worthy, D. E. J., Chan, E., Ishizawa, M., Chan, D., Poss, C., Dlugokencky, E. J., Maksyutov, S., and Levin, I.: Decreasing
846 anthropogenic methane emissions in Europe and Siberia inferred from continuous carbon dioxide and methane observations
847 at Alert, Canada, *J. Geophys. Res. Atmos.*, 114, <https://doi.org/10.1029/2008JD011239>, 2009.
- 848 Yang, X., Tang, J., Mustard, J. F., Lee, J.-E., Rossini, M., Joiner, J., Munger, J. W., Kornfeld, A., and Richardson, A. D.:
849 Solar-induced chlorophyll fluorescence that correlates with canopy photosynthesis on diurnal and seasonal scales in a
850 temperate deciduous forest, *Geophys. Res. Lett.*, 42, 2977–2987, <https://doi.org/10.1002/2015GL063201>, 2015.

- 851 Yi, Y., Kimball, J. S., Chen, R. H., Moghaddam, M., Reichle, R. H., Mishra, U., Zona, D., and Oechel, W. C.: Characterizing
852 permafrost active layer dynamics and sensitivity to landscape spatial heterogeneity in Alaska, *Cryosphere*, 12, 145–161,
853 <https://doi.org/10.5194/tc-12-145-2018>, 2018.
- 854 Yi, Y., Kimball, J. S., Chen, R. H., Moghaddam, M., and Miller, C. E.: Sensitivity of active-layer freezing process to snow
855 cover in Arctic Alaska, *Cryosphere*, 13, 197–218, <https://doi.org/10.5194/tc-13-197-2019>, 2019.
- 856 Zhang, Y., Joiner, J., Alemohammad, S. H., Zhou, S., and Gentine, P.: A global spatially contiguous solar-induced fluorescence
857 (CSIF) dataset using neural networks, *Biogeosciences*, 15, 5779–5800, <https://doi.org/10.5194/bg-15-5779-2018>, 2018.
- 858 Zhang, Y., Commane, R., Zhou, S., Williams, A. P., and Gentine, P.: Light limitation regulates the response of autumn
859 terrestrial carbon uptake to warming, *Nat. Clim. Change*, 10, 739–743, <https://doi.org/10.1038/s41558-020-0806-0>, 2020.
- 860 Zona, D., Gioli, B., Commane, R., Lindaas, J., Wofsy, S. C., Miller, C. E., Dinardo, S. J., Dengel, S., Sweeney, C., Karion,
861 A., Chang, R. Y.-W., Henderson, J. M., Murphy, P. C., Goodrich, J. P., Moreaux, V., Liljedahl, A., Watts, J. D., Kimball, J.
862 S., Lipson, D. A., and Oechel, W. C.: Cold season emissions dominate the Arctic tundra methane budget, *PNAS*, 113, 40–45,
863 <https://doi.org/10.1073/pnas.1516017113>, 2016.

864